Seismic site characterization considering directional near-field seismogenic active faults in Aswan area, Egypt

Mostafa Thabet[1,4] · Khaled Omar[2] · Abdel Nasser Mohamed[2] · Mohamed Osman[3]

Abstract

Aswan area in South Egypt experiences continuous seismic activity due to seismogenic active faults, particularly Kalabsha and Seiyal active EW faults. The seismic site characterization is not properly identified, although the presence of high-density distribution of earthquake stations. The present study investigates fourteen earthquake stations of the Egyptian National Seismic Network, as well as six microtremor measurement sites. We analyzed ground motions due to seismogenic active faults recorded at surface from these fourteen earthquake stations. We measured microtremors for up to 120 min with portable seismometers at six sites in the vicinity of the High Dam area. The horizontal-to-vertical spectral ratios of earthquakes (EHVSR) and microtremors (MHVSR), their plots as a function of frequency and direction of motion, and diffuse field inversion are used in the study. Therefore, we could provide an obvious understanding of the site characterization including resonance frequencies, directional amplifications, and back-calculated subsurface velocity structures at these stations and sites. We found three predominant amplification directions of NS, EW, and NE–SW due to the horizontal components of the seismic waves. These amplification directions are near-transversal ~ transversal to the NS and EW strikes of the active fault system in the study area. In time–frequency analyses of the records, this directionality is observed clearly for S-wave and surface wave time windows. We validated the diffuse field inversion process not only using fitting between observed and inverted EHVSRs and MHVSRs, but also using available geological 2D cross sections and hydrological information in Aswan area.

Introduction

In south of Egypt, many metropolitan areas, and megastructures (e.g., High and Aswan Dams, and Benban Solar Park) are built near Aswan Governorate. Benban Solar Park is currently the fourth-largest solar power plant in the world.

✉ Mostafa Thabet
   mostafa.thabet@aun.edu.eg

1 Geology Department, Faculty of Science, Assiut University, Assiut 71516, Egypt

2 National Research Institute of Astronomy and Geophysics, Helwan, Cairo, Egypt

3 Geology Department, Faculty of Science, New Valley University, New Valley, Egypt

4 Disaster Prevention Research Institute (DPRI), Kyoto University, Kyoto, Japan

A realistic quantification of the seismic site characterization is necessary for an efficient assessment of seismic hazards that is related to the seismic damage. The active fault zones affect the estimation of earthquake seismic hazard, and consequently evaluating the seismic risk analyses. The seismic site characterization due to fault zones has important implications on earthquake hazard causing amplified motions near faults due to guided waves, which in turn increase seismic damage. Pioneering studies conducted by Li et al. (1990; 1994) on the San Andreas Fault zone to analyze guided waves related to fault zone increase the interest toward this field. Reinforced interference of seismic waves in fault zones is strongly responsible for generating high amplification and dispersive energy starting from S-waves to later seismic arrivals (Ben-Zion and Aki 1990; Igel et al. 1997). Additionally, the existence of low-velocity zone (i.e., flower fault structure) is attributed to the fracturing and its subsequent occurrence of fault and clay-rich fault gouge, increased porosity, crack dilatation, pore-fluid concentration, and remineralization (Ben-Zion 1998; Hickman et al. 2005).

Recently, the horizontal-to-vertical spectral ratios (HVSR) of both earthquake (EHVSR) and microtremor (MHVSR) data are used by Rigano et al. (2008), Di Giulio et al. (2009), Pischiutta et al. (2017), Panzera et al. (2017), Burjánek et al. (2012), Panzera et al. (2019), Tortorici et al. (2019), and Kakhki et al. (2020) to reveal the site response related to fault zones. They observed high amplification in the normal direction to the prevailing fault strike. At the Santa Caterina area in Italy, Panzera et al. (2020) studied the site response using the tectono-stratigraphic setting, and they observed high directional HVSR amplification of eight in the normal direction of the dominant North–South fracture zone. At the Victoria fault in Malta, high directional HVSR amplification could not been observed by Villani et al. (2018) through their geophysical investigation, which is a contradict to the previous studies. Their results were interpreted and connected with the present fault zone inactivity (*i.e.,* expressed as ~ 0.6 Myr ago). Along the Vado di Corno fault in Italy, Pischiutta et al. (2017) observed a prevailing high amplification in the normal direction to the active normal faults, which occurred during the L'Aquila 2009 earthquake. Moreover, strong directional horizontal amplification at 1 Hz is observed from microtremor measurements and close to the Pernicana highly fractured fault zone, Mount Etna, Italy (Di Giulio et al. 2009). The distribution of earthquake stations along and across both active and inactive fault zones provides a good possibility to identify fault zone-related site response. Modest variations in geotechnical and/or physical properties of fault zone (e.g., fault length, fault width, velocity contrasts between fractured and unfractured rocks, and seismogenic depth and extent) could produce guided waves (Fohrmann et al. 2004). A small set of waveforms is used by Li et al. (1990; 1997) to investigate the fault zone guided waves up to 100 m wide of low-velocity fault structure, which is extending to the seismogenic depth. Shallow fault zone could generate guided waves, and consequently intense directional horizontal amplification because of very deep ground motions and outside the fault zone (Fohrmann et al. 2004).

Considering these valuable previous studies, the present paper is presenting seismic site characterization due to directional active fault structures at Aswan area in south of Egypt. In this paper, we contribute a detailed analysis of ground motion directionality in site response observed using dataset of 14 earthquake stations and 6 microtremor measurement sites. We analyze the seismic records obtained at both earthquake stations and microtremor measurement sites. First, site response is estimated using the most common HVSR technique. Our findings show significant directional high horizontal amplification, which we consider as being the

related effects of the existence of active fault zones in the study area. The dominant directions of fault zones in south of Egypt, and particularly at the study area, are North–South (NS) and East–West (EW). Here, we explain that the directionality is highly exhibited when the data are rotated in the directions parallel and perpendicular to the fault zones. In addition, the seismic site characterization is predicted in theoretical modeling using diffuse field concept of both earthquake scheme (Kawase et al. 2011; Nagashima et al. 2014) and microtremor scheme (Sánchez-Sesma et al. 2011a). Our back-calculation results are reliable because of the reasonable degree of fitness between predicted HVSR curves and their corresponding observed curves, accompanied with reasonable inference when superimposed with regional geological, tectonic, and hydrological setting in Aswan area. Finally, we provide an updated seismic site characterization associated with the resulting ground motion directionality at each station and site in the study area.

Geological and tectonic setting

As depicted in Fig. 1 (modified after EGSMA 1981), different geological features are existed in the study area. The marine limestone and chalk Sinn El-Kaddab plateau is broad, flat Eocene bedrock at surface, remote region elevating 300–350 m above the Nile Valley, and structurally influenced by the NS and EW fault system (Issawi 1968). The Cretaceous to Eocene layers that underlie the plateau are exposed east of the plateau and in the bordering scarps, which include shales of the Dakhla and Esna Formations; shale, marl, and limestone of the Kurkur, Dungel, and Garra Formations. The Cretaceous to Eocene Nubian formation underlies the plateau, which is composed of sand and sandstone interbedded with clay and shale, and uncomfortably overlies the Precambrian granite basement. This basement is exposed east of the study area as Aswan hills due to uplifting and regional faulting (Issawi 1968). Gabal Marawa is a cap of resistant limestone and exposed on the very low-relief Nubian plain with 274 m elevation (Issawi 1978).

As exhibited in Fig. 2, the study area is dominated by late Cenozoic NS and EW orthogonal strike-slip fault system (Stern and Abdelsalam 1996; Thurmond et al. 2004). The slip rates of EW faults are ≈ 0.03 mm/year, whereas those of NS faults are 0.01–0.02 mm/year. The age of the EW and NS faults is still a controversy (Hamimi et al. 2018). The northwest faults are considered as inactive faults (e.g., Dabud fault). The EW faults are Seiyal and Kalabsha faults, whereas the NS faults are Gable El-Barqa, Kurkur, Khor El-Ramla, Abu Dirwa, and Gazelle faults
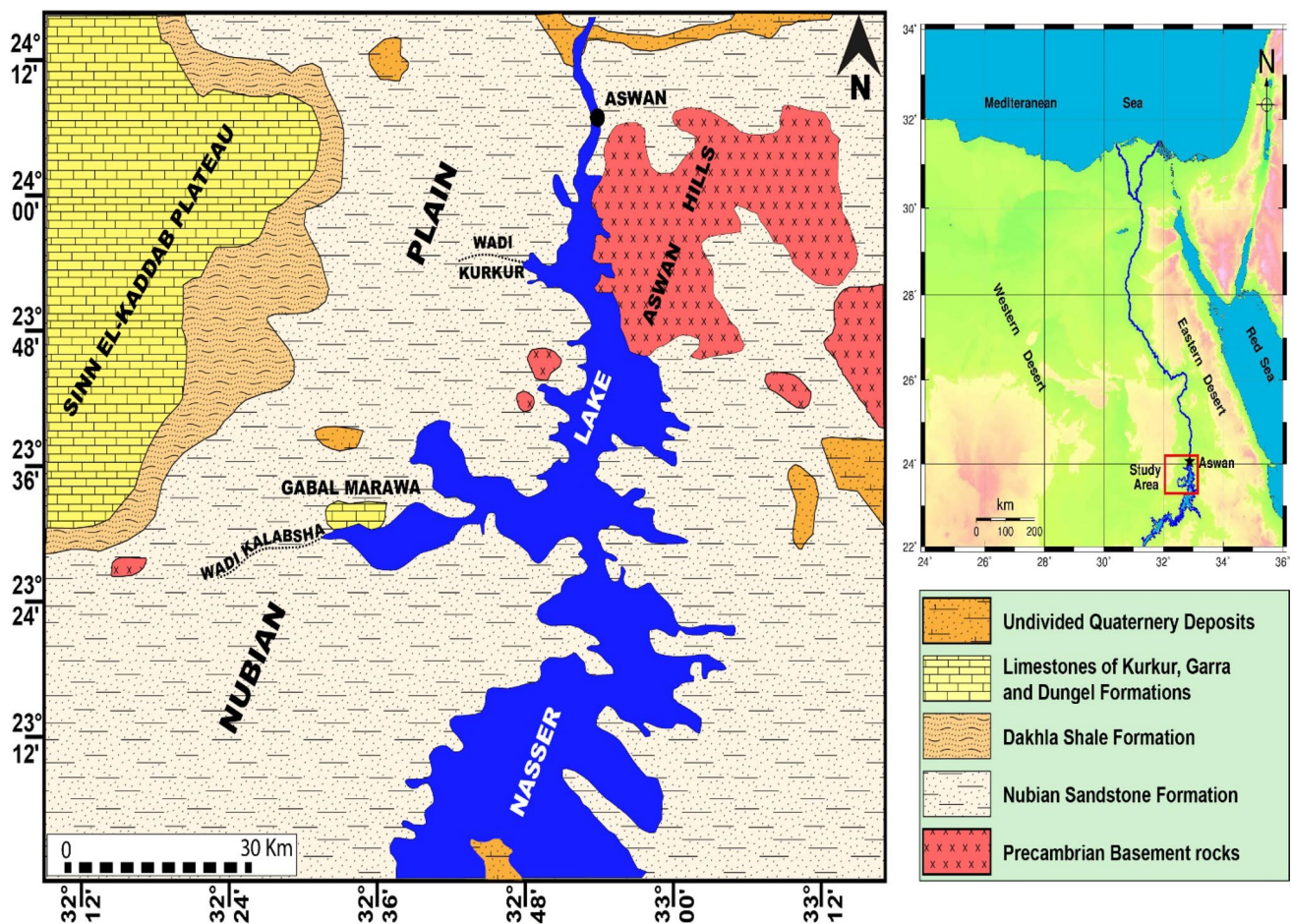
Fig. 1 Geological map of the study area modified after, EGSMA (1981)

(Isswai 1978). This orthogonal fault system was reactivated during two compressional events of the Santonian and late Eocene events (Guiraud and Bosworth 1999). Kalabsha and Seiyal faults are 12 Km apart and have a right-slip movement. The slip rates of the EW faults are ≈ 0.028 mm/year and maximum expected magnitude values are 7 M_S. Left lateral strike-slip movement is prevailing along Gabal El-Barqa, Kurkur, Khor El-Ramla, Abu Dirwa, and Gazelle faults. The slip rates of the NS faults are ≈ 0.006 mm/year, and maximum expected magnitude values are 6.25 ± 0.25 M_S. The NS fault system has very low degree of seismic activity compared with the EW fault system in the region. At the intersection area between Kalabsha and Khor El-Ramla faults, numerous microearthquakes are observed due to deep interactions between the two faults (Fig. 2).

Because of rise in Nasser Lake level, the groundwater levels in the Nubian formation, which is the largest groundwater reservoir in Egypt, are rising, too, due to lake seepage. At the study area, numerical modeling for the groundwater depth in the reservoir has shown variation from ≈ 68 to 106 m (Woodward Clyde 1985), whereas Kim and Sultan (2002) estimated 160 m depth. The eastern end of the Kalabsha fault and segments of the Khor El-Ramla fault submerged in the lake, where maximum pore-pressures of 7 bars. They suggested that the fractured basement has high effective hydraulic conductivity and low effective storage coefficient, and consequently affecting seismic activity in the study area (Omar et al. 2019).

Data set

Earthquake data from the Egyptian National Seismic Network (ENSN) are obtained. Only 21 seismogenic events occurred in the period between 2007 and 2020 are selected
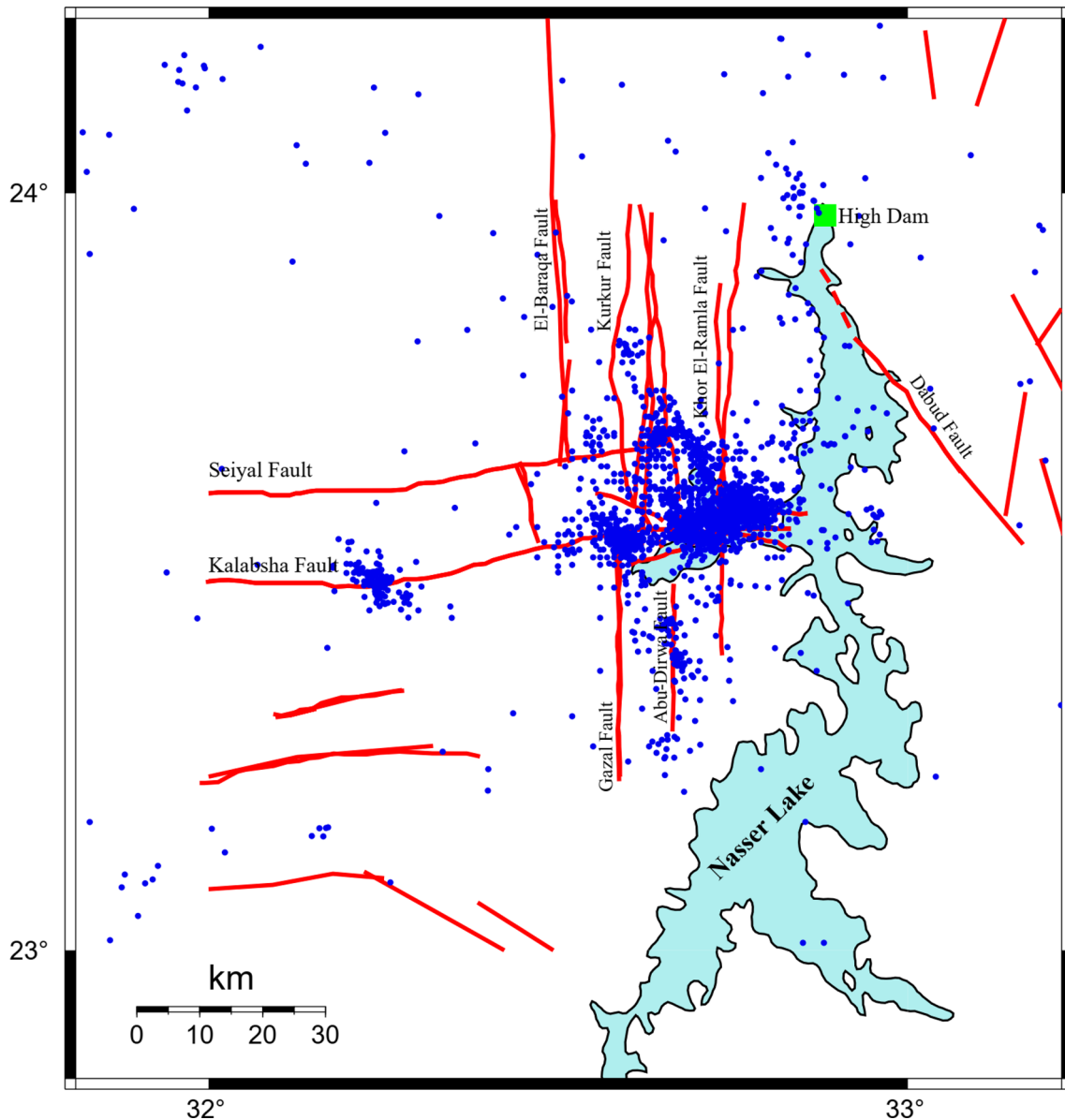
Fig. 2 Tectonic map of Aswan area (red lines are fault traces), accompanied with epicenters of approximately 10,000 earthquakes (blue circles) recorded between 2000 and 2021

and studied in the present research work (Table 1). These seismic events have moment magnitude (M_w) between 3.0 and 4.6 and depths between 0.35 km and 16 km recorded at 14 seismic stations, as shown in Fig. 3. Each earthquake station is installed on surface and instrumented with a three-component Trillium 40 or Trillium 240 seismometer, recording with sampling frequency rate of 100 Hz. The epicentral

locations and magnitudes of these events are obtained from the ENSN catalog.

The waveform quality of each ground motion was tested using signal-to-noise ratio (SNR, Eq. 1), with defining the pre-event and the whole signal windows based on the onset arrival time of *P*-wave. Figure S1 is showing examples of Fourier amplitudes of signal and noise at two stations with

Table 1 List of earthquakes used in the present analysis. (**Sta.**) indicates the numbers of stations out of the 14 stations that recorded each earthquake

No.	Date/time	Lat.	Long.	Depth (km)	Mag.	Sta.
1	2007/04/12 14:17:41.20	23.573	32.695	7.00	3.0	1
2	2007/04/12 14:19:22.60	23.572	32.698	8.30	4.2	1
3	2010/06/22 08:22:07.23	23.716	32.629	0.35	3.2	7
4	2010/11/07 09:54:34.15	24.002	32.847	2.00	4.6	7
5	2010/11/16 02:37:25.55	23.579	32.773	3.08	3.2	4
6	2010/11/30 10:23:26.02	23.563	32.788	3.38	3.0	7
7	2011/02/19 13:59:27.90	23.357	32.681	10.97	3.2	8
8	2011/04/14 06:53:23.37	23.590	32.754	0.44	3.1	8
9	2011/05/12 09:06:55.73	23.577	32.787	0.30	3.2	8
10	2011/06/13 08:08:10.64	23.457	32.593	16.00	3.3	8
11	2012/09/12 18:36:58.47	23.539	32.711	9.58	3.0	14
12	2013/05/17 10:39:27.49	23.668	32.712	3.22	3.2	13
13	2013/06/18 09:26:49.40	23.576	32.720	3.28	3.1	13
14	2013/06/19 16:21:24.94	23.581	32.781	5.03	3.1	13
15	2013/10/27 13:21:43.20	23.566	32.731	0.35	3.4	13
16	2014/02/02 13:31:24.32	23.369	32.675	3.53	3.5	10
17	2014/10/18 10:55:32.17	23.575	32.789	1.96	3.1	9
18	2014/10/18 22:02:09.35	23.578	32.786	1.41	3.0	9
19	2015/11/21 10:47:04.08	23.585	32.780	3.60	3.2	12
20	2015/11/21 10:53:23.00	23.581	32.783	4.13	3.1	12
21	2020/08/15 03:49:57.82	23.579	32.714	8.70	3.3	8

the nearest and farthest hypocenter distances. Accordingly, waveforms having SNR greater than 2 in all the frequency bands of 0.1–1.0 Hz, 0.1–10.0 Hz, and 0.1–30.0 Hz are used to ensure that only accepted quality waveforms are included in the further analyses.

$$SNR = 10LOG_{10}\left(\frac{\sum S^2}{\sum N^2}\right), \qquad (1)$$

where N is the pre-event Fourier amplitude, and the S is the whole signal Fourier amplitude.

Microtremor data are obtained from field measurements carried out during two field campaigns in the winter seasons of 2019 and 2020 at six sites in the study area (Fig. 3) using three-component Trillium Compact 120s seismometer and a Taurus Portable recorder. These field measurements were avoided during the mid-day periods to ensure the most appropriate conditions for operating the instruments (*i.e.,* temperature $\approx 23°C$). Other precautions were considered too, such as avoiding external wiring, windy days, and recording nearby heavy vehicles. Figure S2 is showing an example of raw and filtered time series of microtremor measurements at site A and accompanied by field measurement's

photo. Continuous background noise measurements were recorded for duration between 60 ~ 120 minutes during daytime at each measurement site with a sampling frequency rate 100 Hz.

Methodology

Earthquake data processing

We studied 21 earthquakes with phase windowing of only *S*-waves and coda waves. Previous studies concluded limited dependence of the data sensitivity on the signal window duration (e.g., Douglas et al. 2010; Ktenidou 2010). In the present study, the window's length is 100 s and must be tapered to ensure the infinite signal assumption when performing the Fourier transform on a finite window. The onset arrival time of *S*-waves is manually picked; thus, this will guarantee accurate delimitation of the phase windows. The selection of this constant phase window duration (W_d) of 100 s is mainly depending on the fact that the fundamental resonance frequency must be greater than ten times
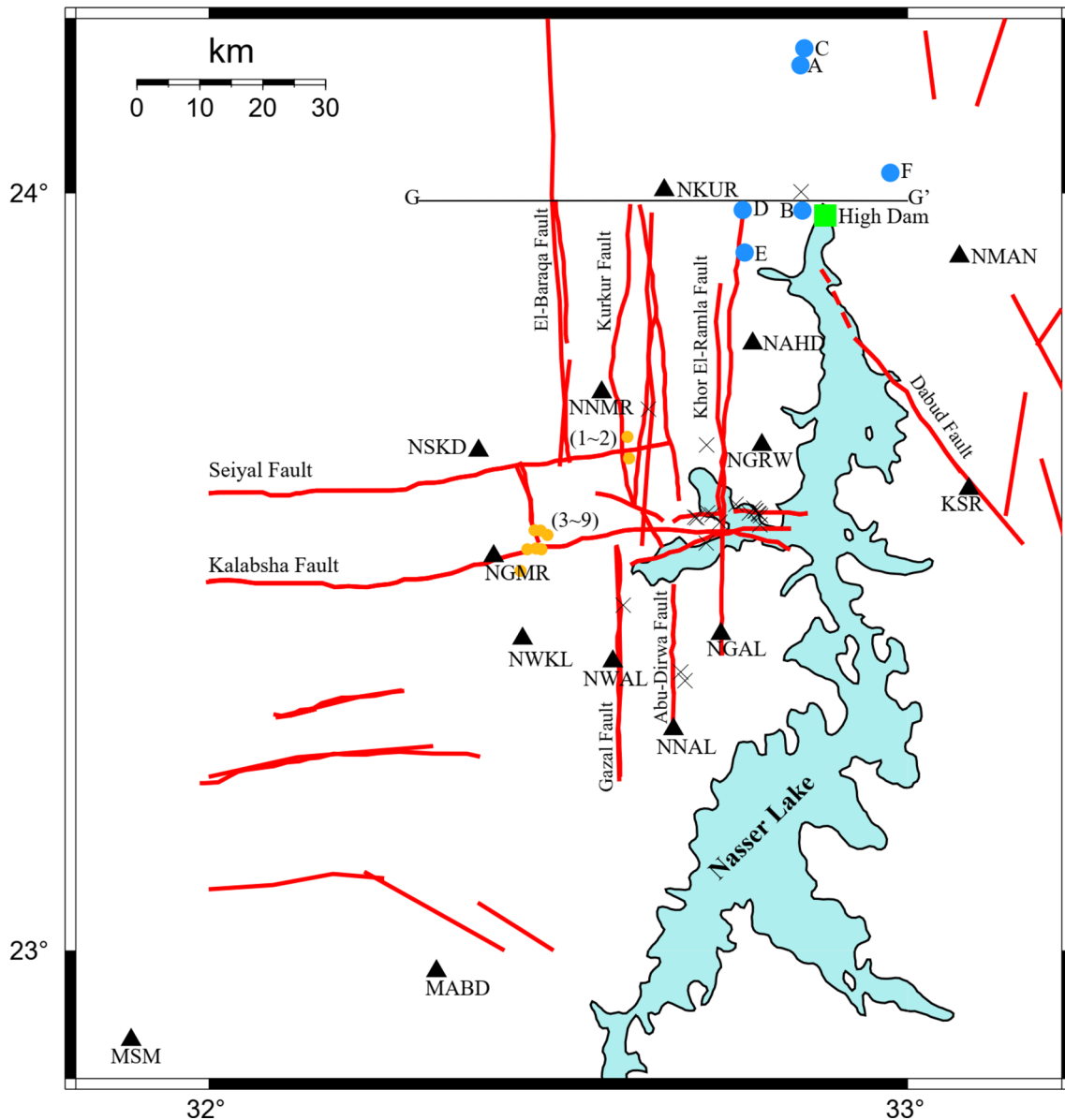
Fig. 3 Location map for the earthquake stations (Black triangles), the microtremor measurement sites (blue circles), the fault traces (red lines), the 21 seismic events used in the present study (black crosses), the 1–9 boreholes for groundwater data (orange circles), and GG' line is a geological 2D cross section obtained from Mekkawi et al. 2005 and plotted in Fig. 15

the significant cycles (i.e., wavelengths) in each window. For example, a window length of 100 s contains only ten wavelengths of period 10 s. If the number of wavelengths (S_c) necessary to secure an acceptable Fourier spectral resolution, then the minimal reasonable frequency (f_m) for the Fourier amplitude spectra is given by Eq. 2:

$$f_m = S_c/W_d. \tag{2}$$

Earthquake waveforms in the present study were baseline corrected and bandpass filtered in the range 0.1–30.0 Hz using Butterworth filter prior to calculating the Fourier spectra applying 5% cosine-tapering window function.

The Fourier spectra are smoothed using a Konno–Ohmachi (Konno and Ohmachi 1998) window with a constant smoothing parameter, $b = 40$. Thus, the important information in each spectrum will be secured for further diffuse field inversion process. Because the algorithm of diffuse field inversion (Kawase et al. 2011; Nagashima et al. 2014) processes the EHVSR applying geometric mean, the present EHVSRs are calculated with applying geometric mean on all obtained spectral ratios for each earthquake at each station. This will result in one representative EHVSR curve for each station. Finally, the time–frequency spectrograms and the directional rotated EHVSRs are calculated at each earthquake station using GEOPSY software suite (Ver. 3.3.3, Wathelet et al. 2020, http://www.geopsy.org). For calculating directional rotated EHVSR, we use the same b parameter of 40. The inter-earthquake variability among EHVSR spectra, which resulted from using different earthquakes, has been evaluated to check the confidence level of the present data. The following series of equations are adapted to evaluate this inter-earthquake variability between different EHVSR spectra $s(f)$.

$$\mu_{ln} = \frac{1}{n} \sum_{i=1}^{n} ln\left[s_i(f)\right], \tag{3}$$

where $s_i(f)$ is the $s(f)$ for the $i = 1, \dots, n$ earthquakes, and the index of ln is describing the natural logarithm.

$$\hat{s}(f) = \exp\left[\mu_{ln}\right] \tag{4}$$

$$\sigma_{ln}(f) = \sqrt{\frac{1}{n} \sum_{i=1}^{n} \left(ln\left[s_i(f)\right] - ln\left[\hat{s}(f)\right]\right)^2} \tag{5}$$

This inter-earthquake variability occurs because difficulties to separate the site response away from the associated source and path responses. Because the values of σ are calculated at each frequency point $\sigma(f)$, so that, the median and mean of these values of σ are used to quantify this inter-earthquake variability. These values are necessarily arbitrary and their exact threshold values are controversial.

Microtremor data processing

The microtremor time series have sampling frequency rate of 100 Hz and a duration of 60–120 min from each measurement site is processed using GEOPSY software suite (Ver. 3.3.3, Wathelet et al. 2020, http://www.geopsy.org) to determine the MHVSR curves and their directional rotated MHVSR. Each microtremor time series is subdivided into unoverlapping time windows of 100 s. Certainly, the longer the selected subdivided time window, the higher the number of significant cycles or wavelengths considered for the

Fourier spectra at the lowest analyzed frequency. Consequently, the criteria and guidelines suggested by the European research project of SESAME (Bard and SESAME team 2004) are followed and fulfilled. As is the earthquake data processing, the waveforms are bandpass filtered in the range 0.1–30.0 Hz using Butterworth filter with applying 5% cosine-tapering window function at both start and end of the time series. Based on fixed short time average (STA = 1 s) over long time average (LTA = 30 s), only the most stationary parts, which are less influenced by nearby or time-varying noises, are extracted, whereas the transients associated with nearby noise sources are eliminated. This step executed depending on visual inspection for all the time series waveforms. Smoothing filter on the computed Fourier spectra of each time window is applied using Konno–Ohmachi window, with the b parameter of 40. Also, for calculating directional rotated MHVSR, we use the same b parameter of 40. The resulting spectra of the geometric mean of the horizontal components are divided by their corresponding spectra of the vertical component in each time window. The final MHVSR for each measurement site is calculated by taking the mean of the logarithmic MHVSRs obtained from all the time windows.

When possible, the fundamental frequencies (first frequency) are picked on the resulted six MHVSR curves. Verification of the stability of fundamental frequency and its peak amplitude is tested in compliance with criteria of Bard and SESAME team (2004). These criteria include fundamental frequency (f_0) < 10 significant cycles, the significant cycles ≥ 200, and low standard deviation for amplitude (≤ 2 or ≤ 3 for $f_0 > 0.5$ or < 0.5 Hz, respectively).

Back-calculation of velocity structures

The back-calculation of P- and S-wave velocity structures is executed based on two diffuse field inversion schemes specifically designed for EHVSR and MHVSR. Since microtremors consist of mainly surface waves from randomly distributed point sources on the surface, so that, it is necessary to use the imaginary part of the Green's function at the same location of the observed site to obtain the diffusive

Table 2 Initial subsurface P- and S-wave velocity structure (i.e., V_p and V_s) of Aswan area

Kebeasy et al. (1991)			Mohamed et al. (2015)	
V_P (km/s)	V_S (km/s)	Thickness (km)	V_P (m/s)	Thickness (m)
2.1	1.22	0.25	873–1341	5–10
5.1	2.85	3.4	2164–2467	20–25
5.2	3.2	3.3		
6.35	3.55	8.1		
6.8	3.77	12.2		

energy density spectra (Sánchez-Sesma et al. 2011a). On the other hand, earthquake ground motions consist of mainly body waves, particularly, the *S*-wave portion from the deep sources is diffused. Kawase et al. (2011) showed that the resulting final representative EHVSR curve using many earthquakes should be calculated as the ratio of the absolute value of the *S*-wave transfer function with respect to that of the *P*-wave transfer function with a constant that corresponds to the equipartition of energy at the seismological bedrock.

Eventually, the relevant interpretation of the diffuse field concept in Sánchez-Sesma et al. (2011a) for MHVSR and Kawase et al. (2011) for EHVSR should be discriminated from each other, because the nature of seismic wavefields and their predominant incident wave types are different. Lermo and Chavez-Garcia (1994) and Field and Jacob (1995) do not recommend similarity between EHVSRs and MHVSRs. Recently, Mori et al. (2015) established detailed comparisons between EHVSRs and MHVSRs through studying *S*-wave velocity inversion using pseudo-MHVSRs.

In the present study, *P*- and *S*-wave velocity structures are examined and back-calculated beneath each earthquake station using EHVSR inversions running by FORTRAN code program developed by Nagashima et al. (2014), which is specifically designed for calculating the theoretical EHVSR based on the diffuse field concept.

Beneath each microtremor measurement site, the subsurface velocity structures are back-calculated using MHVSR inversions running by HV-Inv, which is a MATLAB code program developed by García-Jerez et al. (2016). Depending on the diffuse field approximation (Sánchez-Sesma et al. 2011a), this HV-Inv is designed for calculating the theoretical MHVSR curves. This code program could be obtained from the HV-Inv project website (http://www.ual.es/GruposInv/hv-inv/).

From the literature, the deep and shallow subsurface velocity structures obtained from Kebeasy et al. 1991 and Mohamed et al. (2015), respectively (Table 2), provide an initial guess of the velocity structures and their constraining search space for V_p and V_s to feed into the back-calculated velocity structures. Several initial velocity structures are designed considering gradual increase in velocities from $0 \sim 3000$ m depth. The search space is constrained as $\pm 300\%$ of the initial input velocity structures. Fitting between the observed and inverted EHVSRs and MHVSRs is considered as the main criteria to judge the reliability of the resulted inverted subsurface velocity structures.

Results and discussion

Earthquake stations

Figure 4 exhibits the EHVSR results at the 14 earthquake stations. One of the prominent seismic characterizations is the differences between the differently averaged EHVSRs of both horizontal components (i.e., EW and NS). Accordingly, the 14 stations are exhibiting frequency-dependent EHVSRs for frequencies lower than 10 Hz.

The whole 14 stations are characterized with higher EHVSRs of EW components at frequencies < 2 Hz, whereas both components are comparable at higher frequencies. However, MABD, NGAL, NGMR, and NNMR stations are exhibiting slightly higher EHVSRs of NS components at frequencies > 2 Hz. An exception to this is exhibited by NAHD, which has higher EHVSRs of EW component at all frequency bands. KSR and NWKL stations are excluded because the accepted events used in their averaged EHVSRs are 1 and 2 events, respectively. Their averaged EHVSRs are not considered as stable EHVSRs. According to the values of σ, 12 earthquake stations could be categorized in two groups. MABD, MSM, NAHD, NGMR, NGRW, NKUR, NNAL, and NWAL have values of $\sigma \leq 0.40$. NGAL, NMAN, NNMR, and NSKD have values of $\sigma > 0.40$. The azimuths between the accepted events and the corresponding stations are calculated. After that, we calculated the average and the standard deviation of these azimuths at each station. Figure S3 is showing correlation between the value of σ and the corresponding average and standard deviation. Although the presence of outliers at stations of NNMR, NSKD, and NGMR, we could generally conclude that the value of σ is influenced by the spatial distribution of events and the relative position of each station.

Figure 5 shows an example of the time–frequency analyses at NNMR station. Most of the stations are characterized by concentrated ground-motion energy in the range of 0.5–10.0 Hz. The highest energy source is mainly produced from the time window of the *S*-waves and the consequent Coda waves. The horizontal components have significant contribution in the ground-motion energy whenever compared with the corresponding vertical component. The directionality due to the dominant directions of fault zones in the study area is highly exhibited in the differently polarized horizontal components. For example, NNMR station is showing highly concentrated ground-motion energy in the NS component (Fig. 5). Therefore, we used the rotational
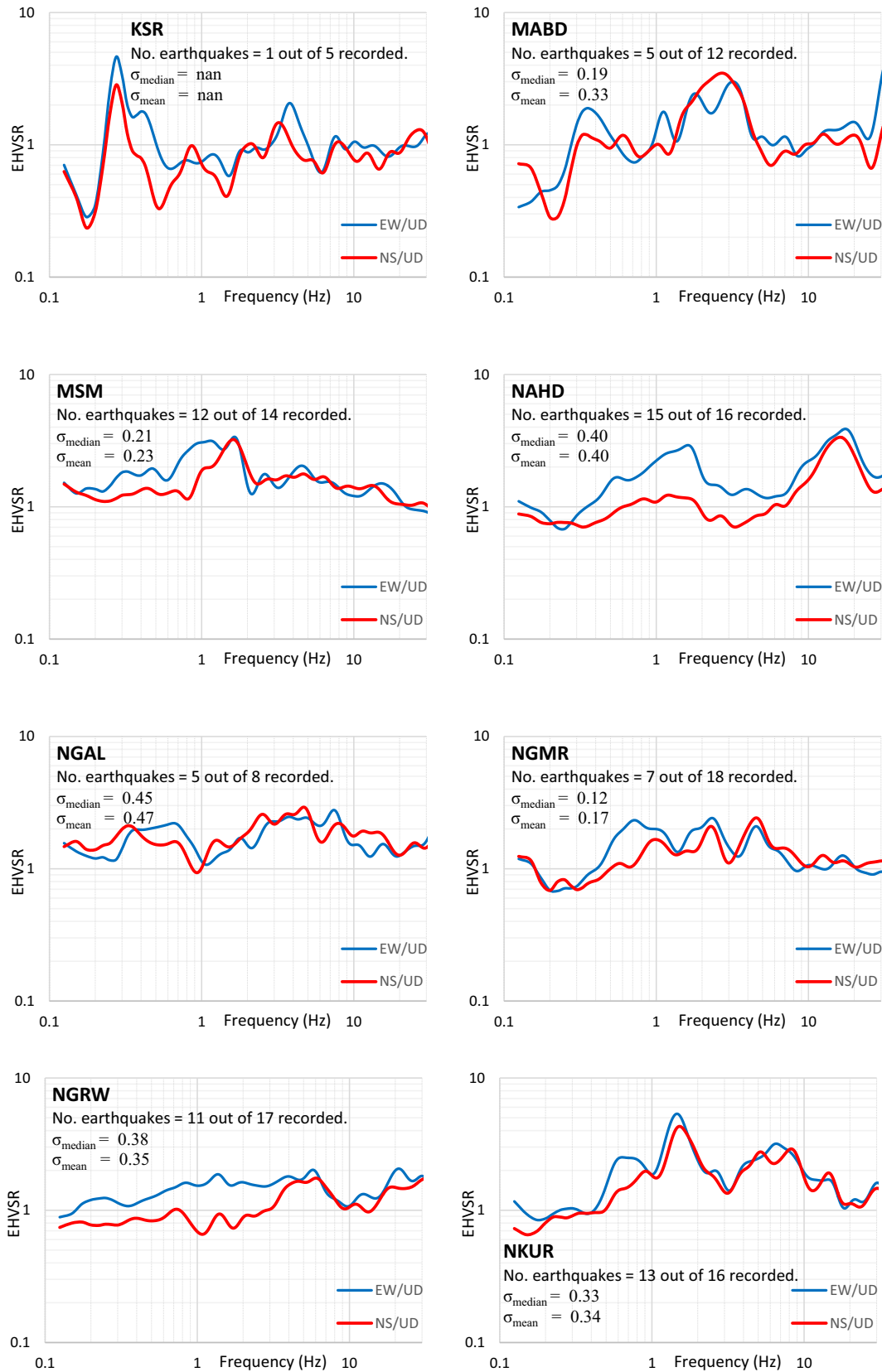
Fig. 4 The averaged EHVSR curves of horizontal components at the 14 earthquake stations. The number of accepted earthquakes out of the recorded earthquakes are given and accompanied by the σ values
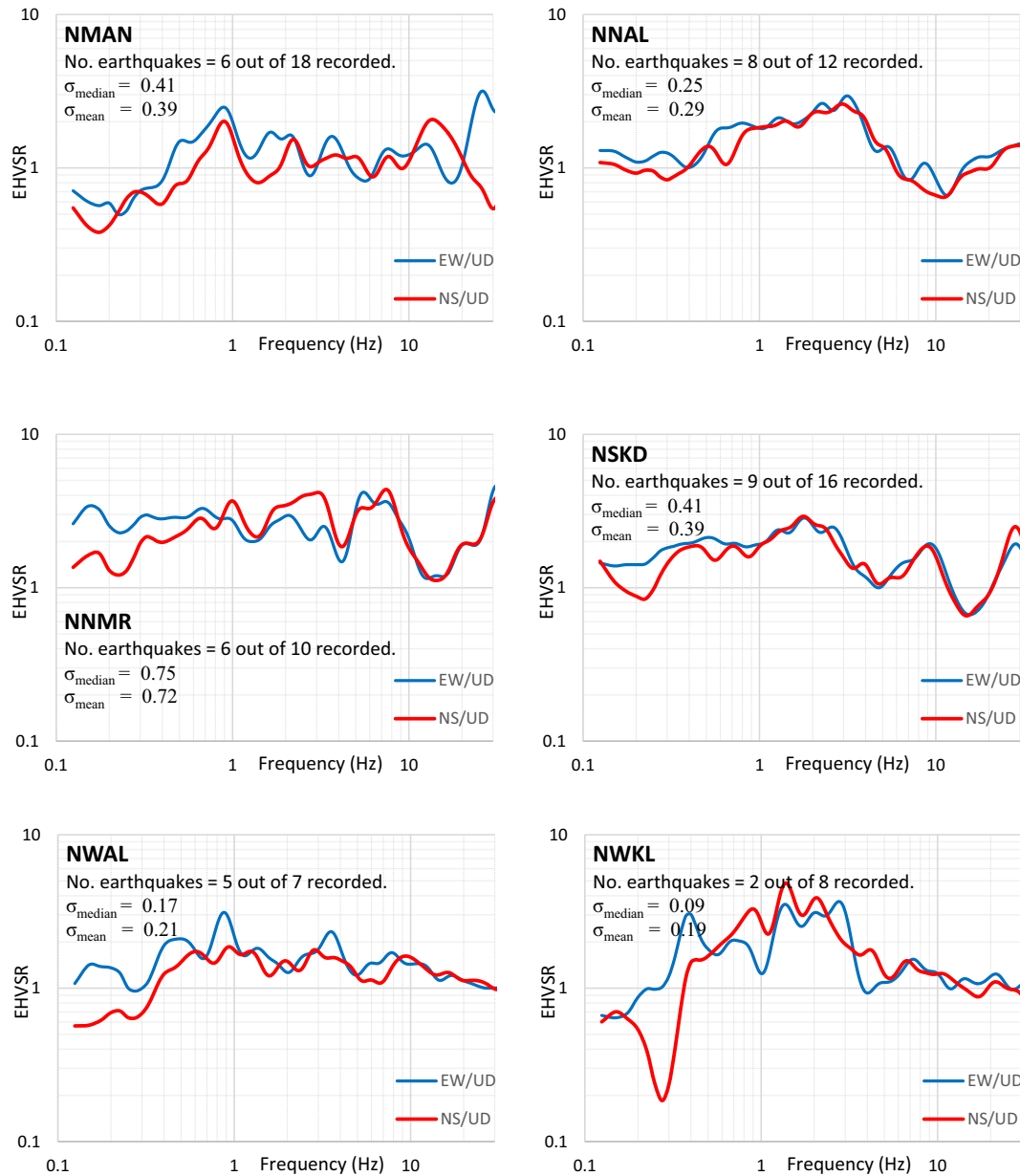
Fig. 4 (continued)

EHVSR plots to conclude the dominant polarized horizontal directions. Figure 6 is exhibiting the achieved plotting results of the observed EHVSR spectral ratios that calculated after rotating the NS and EW horizontal components of motion from 0° (north) to 180° (south), as a function of frequency (x-axis) and direction of motion (y-axis). These rotational EHVSRs are plotted using independent earthquakes having

high *SNR* at each station, because it was difficult to have one common earthquake recorded by all the stations and has accepted *SNR*s. For example, the 11th earthquake in Table 1, which is recorded by all the stations, has accepted SNR at only 3 stations. With regard to the resulting rotational EHVSRs (Fig. 6), it appears that:

Fig. 5 Example time–frequency analyses associated with their corresponding velocity time series for the event 2014/02/02 13:31 of Mag. 3.5 recorded at NNMR station
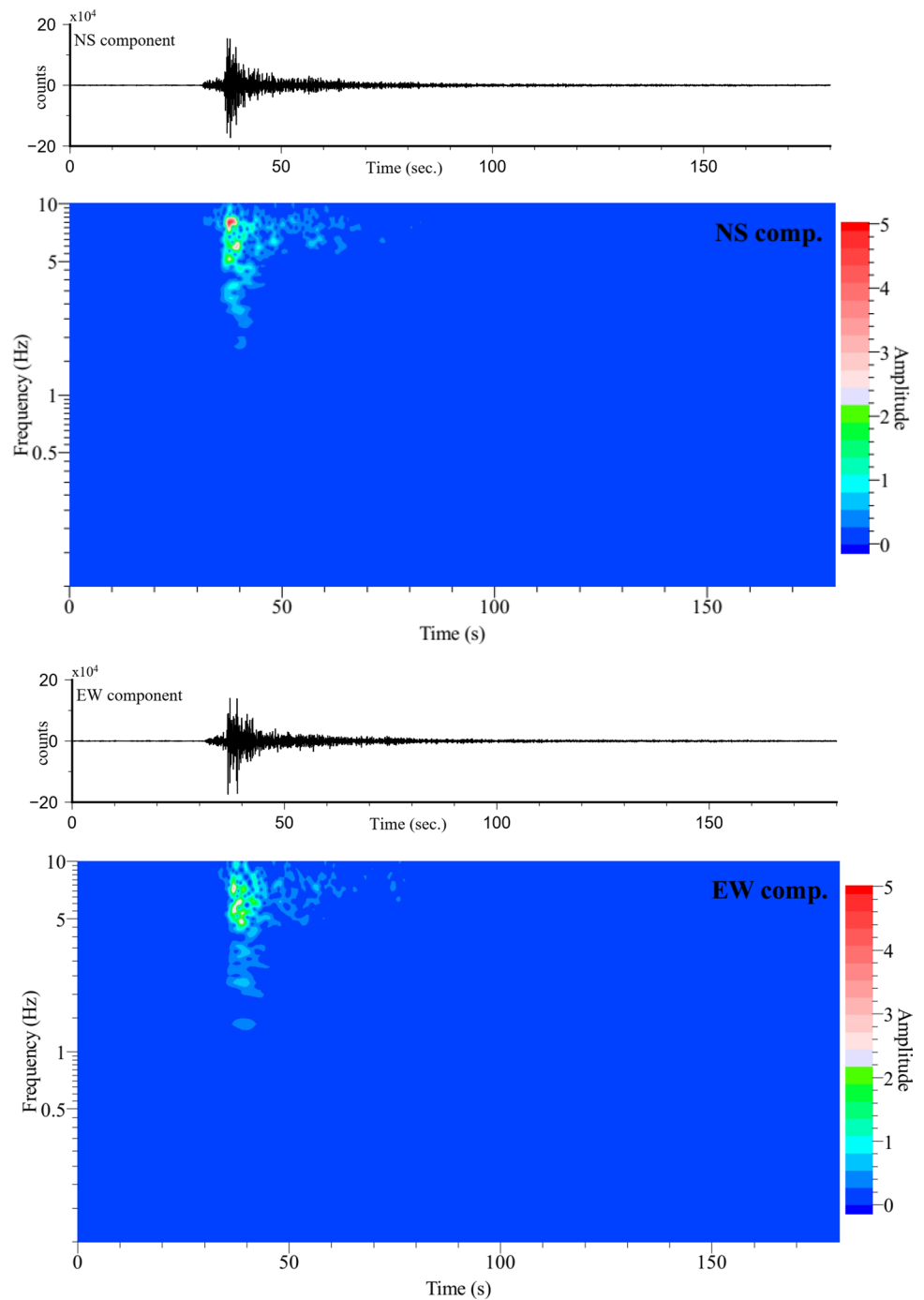
- Stations KSR, MSM, NAHD, NGRW, NNAL, NNMR, and NWAL appear to be characterized by single maximum amplitudes striking EW, and in some cases by maximum multimodal amplitudes (e.g., NAHD and NGRW).

- Stations MABD, NGAL, NGMR, NMAN, NKUR, NSKD, and NWKL appear to be characterized by multimodal maximum amplitudes striking NE–SW, and in

Fig. 5 (continued)
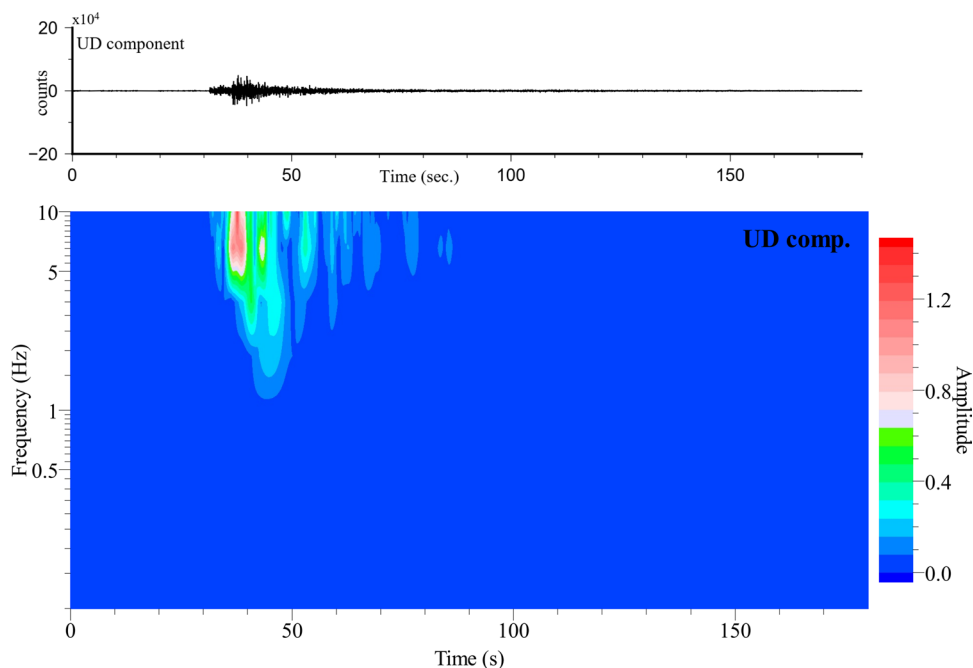
some cases by single maximum amplitudes (e.g., MABD, NMAN, and NWKL).

Table 3 is summarizing the frequency ranges of the strikes of the maximum amplitudes deduced from the achieved rotational EHVSR plots. There are congruences in the concluding remarks between Figs. 4 and 6, particularly in the low frequencies. The used events in this study are distributed on a localized zone in the study area, as shown in Fig. 3. This indicates slight differences among source characteristics and directions. This explains these congruences, despite average EHVSR curves (Fig. 4) are using many events, whereas rotational EHVSR plots (Fig. 6) are using independent events. The high EW amplitudes (Fig. 4) are dominated at frequencies lower than 2 Hz and indicate the presence of significant difference between the polarized horizontal directions due to deep structures. NGRW station is exhibiting its high EW amplitudes up to 6 Hz, whereas at NAHD station, the difference between the polarized horizontal directions is dominant in all frequency bands. This could be attributed to the impact of directionality not only on deep structures, but also on the shallow depths. In the literature (Fäh et al. 2001; SESAME, 2004, Bonnefoy-Claudet et al. 2008), various interpretations

for the EHVSR amplitudes are highly debated considering velocity or impedance contrasts and/or type of waves (e.g., Rayleigh, Love and body waves).

The resulting EHVSRs revealed dominant polarization in EW and NE–SW directions (Fig. 6). The variability in these polarized directions among earthquake stations could be caused by different site characterizations due to NS and EW active fault system in the study area. These dominant polarization directions in EW and NE–SW are transversal–near-transversal to the NS and EW main strikes of the active fault system in the study area (Fig. 3). This relationship between the dominant polarization directions and active fault system agrees with the interpretations in the literature proposed by Pischiutta et al. (2017); Panzera et al. (2020). Moreover, the observed amplification occurs dominantly at frequencies (0.5–8 Hz) higher than the ones produced by the microtremor measurements. The wavelengths approximately equalize the width of the active faults in the study area corresponding to these dominant frequencies. Moreover, the *P*-wave and *S*-wave velocities in the fault zones are approximately 5.10 and 2.85 km/s, respectively (Table 2). Consequently, the estimated wavelengths are ranging between 5.70–0.36 km.
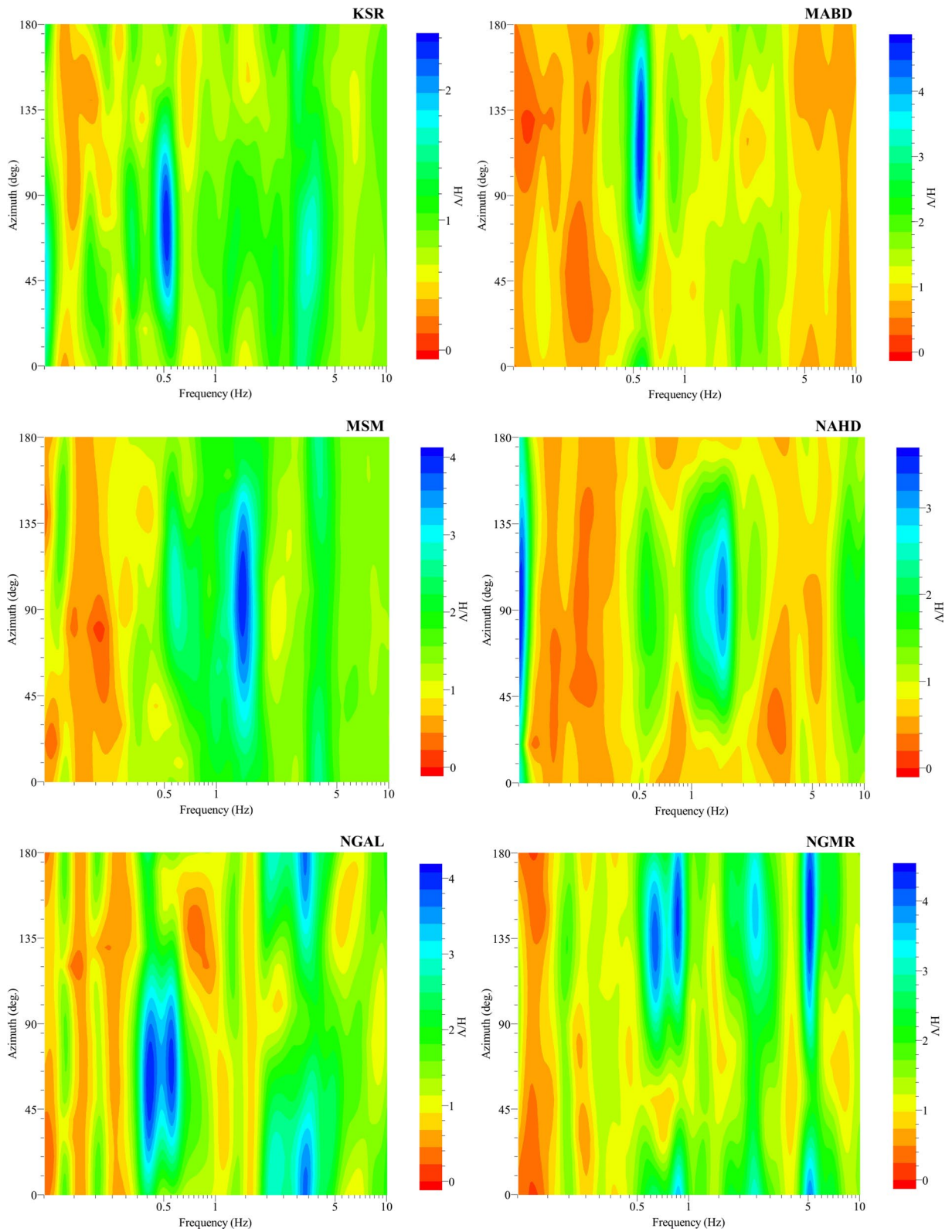
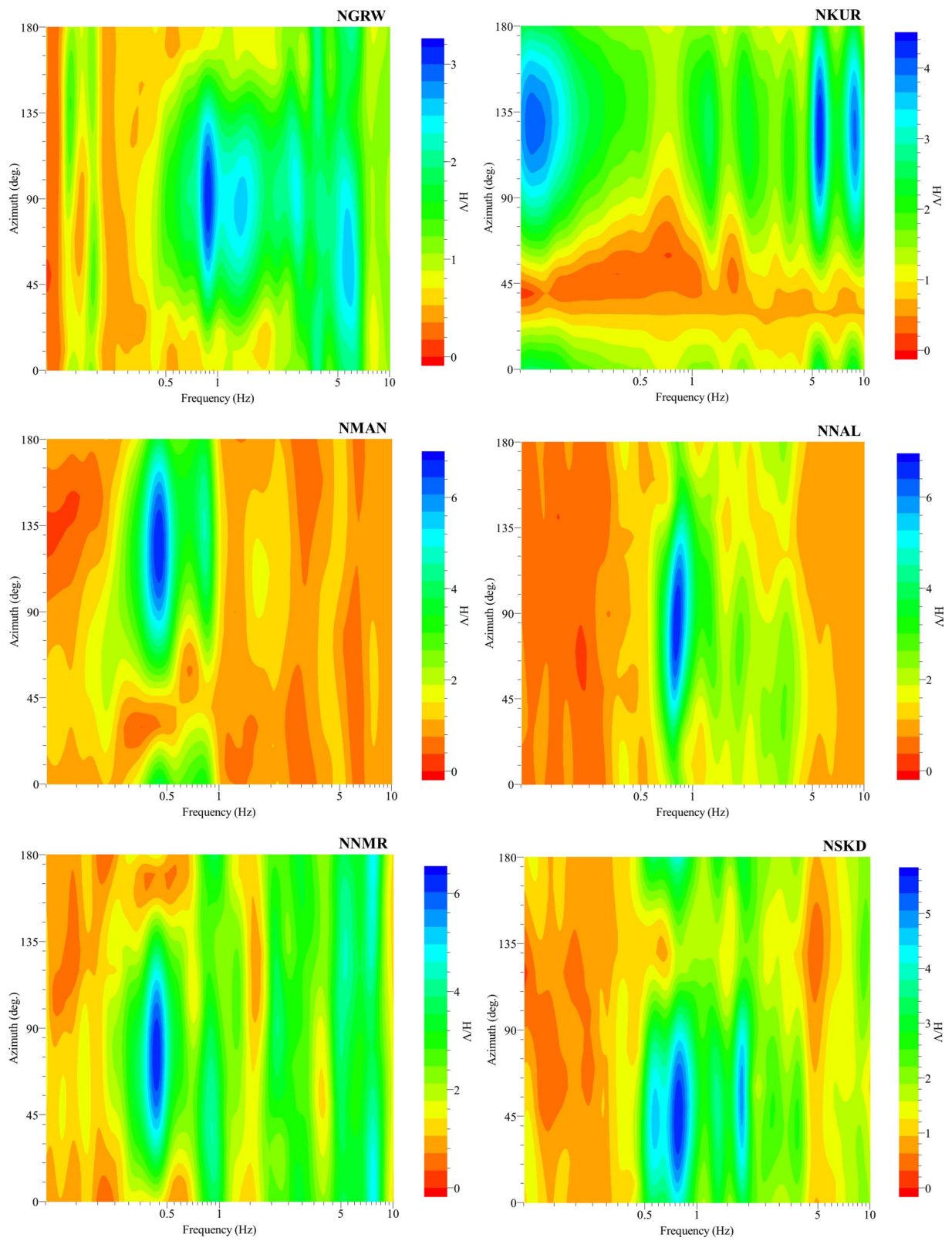**Fig. 6** Rotational EHVSRs at the 14 earthquake stations
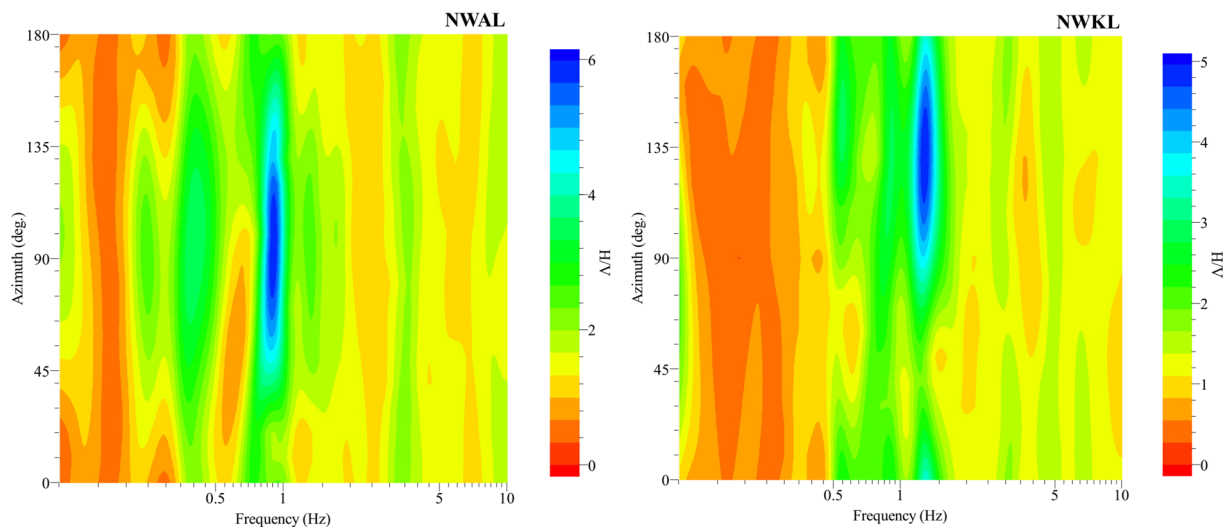
Fig. 6 (continued)

Fig. 6 (continued)

Microtremor measurements

Figure 7 exhibits the MHVSR results at the 6 microtremor measurement sites. These resulting MHVSRs are characterized by fundamental predominant broad peaks in the

Table 3 Summarized strike and frequency as deduced from rotational EHVSR plots

Station	Strike (°N)	Frequency range (Hz)	Peak mode
KSR	45–110	0.40–0.60	Single
MABD	90–150	0.40–0.60	Single
MSM	60–120	1.00–1.50	Single
NAHD	50–110	0.50–1.50	Multimodal
NGAL	0–20	2.00–3.50	Multimodal
	160–180		
	30–90	0.35–0.60	
NGMR	0–10	0.65–1.00	Multimodal
		4.50–5.50	
	110–170	0.65–1.00	
		4.50–5.50	
NGRW	60–110	0.50–1.50	Multimodal
NKUR	110–150	0.15–0.25	Multimodal
		5.00–10.00	
NMAN	0–10	0.35–1.00	Single
	100–150		
NNAL	50–110	0.65–1.00	Single
NNMR	50–110	0.40–0.50	Single
NSKD	0–60	0.50–1.00	Multimodal
		1.50–2.00	
	170–180	0.50–1.00	
		1.50–2.00	
NWAL	60–120	0.70–1.00	Single
NWKL	100–160	1.0–2.0	Single

frequency range of 0.3–1.0 Hz. These sites are exhibiting higher MHVSRs of NS components. An exception is site B, which is exhibiting higher MHVSRs of EW component.

It is important to know that sites A through F are locating in close vicinity and surrounding the High Dam area (Fig. 3). The MHVSRs at sites B, D, E, and particularly site F are exhibiting obvious sharp troughs. These local narrow troughs are occurring at 2 Hz frequency and having industrial origin, which could be related to the anthropogenic sources in Aswan region. According to Bard and SESAME team (2004), we check the Fourier spectra of the individual three components at these sites. Figure 8 is illustrating with an example of raw spectra from each individual component at site F. In site F, clear and sharp peaks are exhibited on all orthogonal components at ≈ 16 Hz, whereas ≈ 2 Hz peak is exhibited only on the UD component. Therefore, we run damping test of the time-domain analyses using the Random Decrement method, which is adopted in GEOPSY software suite. Figure S4 is showing the damping results at site F in the low frequency range of $2.08 \sim 2.09$ Hz and high frequency range of $15.79 \sim 16.20$ Hz. The UD component at frequency 2.08 Hz with very low damping of $\approx 0.17\%$ is only witnessing an anthropogenic source. This conclusion is also verified in the time–frequency analyses of the UD component at site F (Fig. 9). This noise of anthropogenic origin is clear and continuous at ≈ 2 Hz. Sites A and C do not exhibit any of these industrial origin peaks because of their existence outside the impact area of these industrial origin sources (*i.e.*, far away from the High Dam).

As deduced from Fig. 7, peaks of the fundamental resonance frequencies (f_0) are ranging from 0.3–1.0 Hz and not influencing by the industrial noise of the High Dam. In addition, the directionality is obvious in this frequency range. Moreover, the amplitude of the fundamental peaks
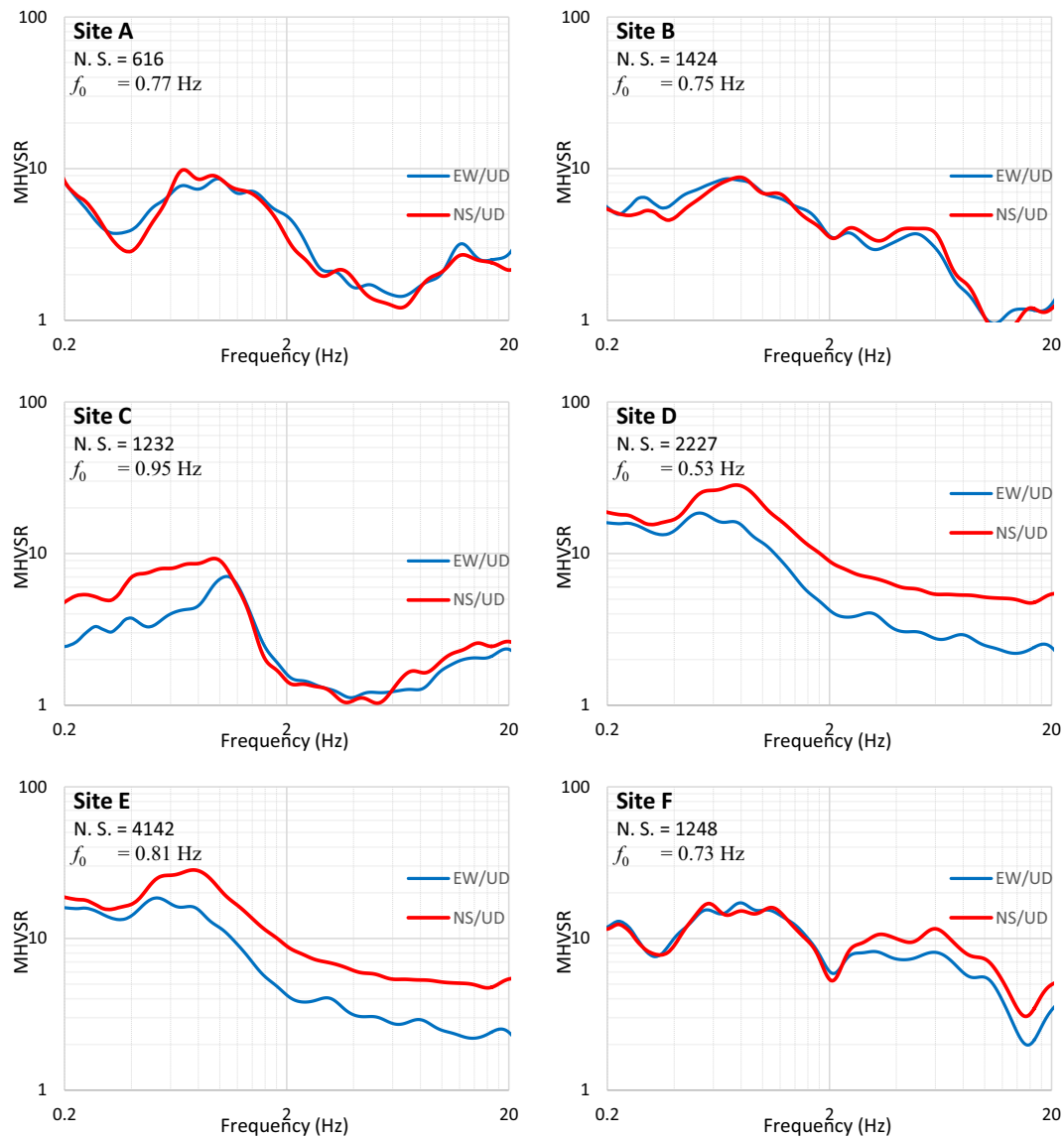
Fig. 7 MHVSR curves of horizontal components at the 6 microtremor measurement sites. The number of significant cycles (N. S.) and the fundamental frequency (f_0) are given

is higher than 2 and decreases to $<$ $<$ half of the amplitude of the fundamental peaks in the frequency range of $f_0/4$–4 f_0. On the other hand, the troughs of frequencies 2 Hz are having industrial origin and existing at sites B, D, E, and F. Therefore, sites B, D, E, and F are excluded from further diffuse field inversion process because of their misleading impact on the back-calculated subsurface velocity structures. According to suggestions for processing and interpretation

by Bard and SESAME team (2004), the resulting fundamental resonance frequencies at the 6 microtremor measurement sites are reliable.

Figure 9 shows the time–frequency analyses of typical three component noise records at site F. The ground-motion energy is concentrated in the low frequency range $<$ 1 Hz and the high frequency range $>$ 5 Hz. Most of the energy is observed in the horizontal components, particularly the NS
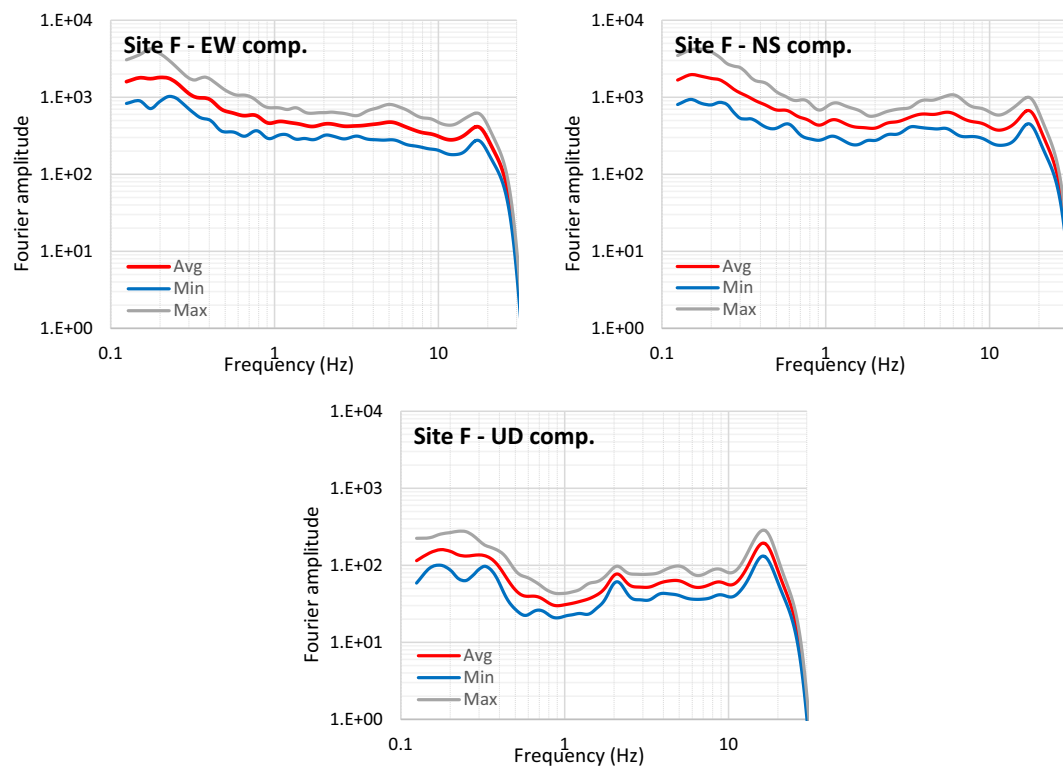
Fig. 8 Fourier amplitudes of the three orthogonal components measured at site F

component. After performing similar time–frequency analyses at the other microtremor measurement sites, consistent characteristics are also resulted.

Figure 10 is exhibiting the achieved plotting results of the experimental MHVSR spectral ratios that calculated after rotating the NS and EW horizontal components. The troughs of industrial origin sources could be eliminated because of using smoothing *b* parameter of 40. From the resulting rotational MHVSRs, it appears that A, C, D, and E sites are characterized by multimodal maximum amplitudes in the frequency range between 0.5 and 1.0 Hz and striking NS (0~40 °N and 140~180 °N). These dominant polarization directions in NS are transversal to the EW main strikes of the active fault system, which are Kalabsha and Seiyal faults (Fig. 3). Site B is an exception and having single maximum amplitudes in the frequency range between 0.5–1.0 Hz and striking NE–SW (30–110 °N), whereas site F has its single maximum amplitudes in the same frequency range and striking NE–SW (110–170 °N).

The difference between the EHVSRs and MHVSRs is attributed to the different nature of the wavefield for the earthquakes and microtremors. Body-wave contribution in EHVSRs is the major sources of earthquakes. Surface wave contribution in microtremors is dominant and work as randomly distributed point sources with several loading directions. See Weaver (1985), Shapiro et al. (2000), Margerin et al. (2009), Sánchez-Sesma et al. (2011b), and Piña-Flores et al. (2021) for references. The existence of a diffuse field must comply with several physical conditions, particularly with the equipartition of energy. Each seismic wave of *P*-, *SV*-, *SH*-, Rayleigh-, and Love-type has a fixed associated energy and is proportional to the number of its modes as in surface waves only. The microtremor record can be viewed as stable random process because the microtremors are generally regular during the recorded day interval.

Remarkably, there are significant differences between EHVSRs and MHVSRs in their frequency and amplitude characteristics regarding the fundamental and/or

Fig. 9 Example time–frequency analyses associated with their corresponding velocity time series recorded at microtremor measurement Site F. (Note that reduced amplitude scale is used for the UD component to observe the industrial origin noise at frequency ≈ 2 Hz)
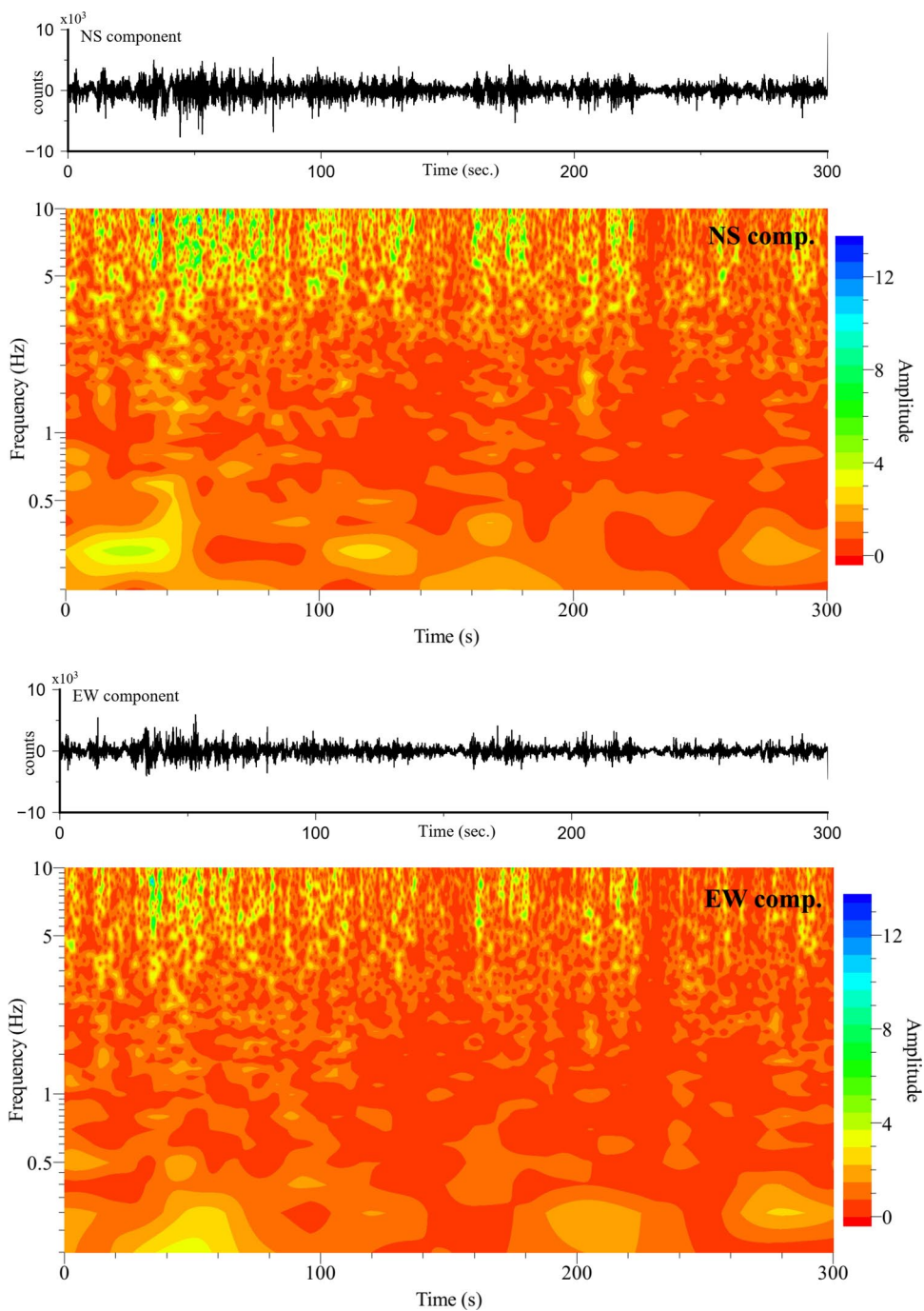

predominant peak frequencies (compare Figs. 4 and 7). This is because EHVSRs are mainly associated with higher modes, whereas surface waves would not severely excited with these higher modes as appear in MHVSRs.

Back-calculated velocity structures

Figure 11 shows the superimposition of observed and inverted EHVSR curves at the 12 earthquake stations. It is important to note that the geometrically averaged observed

Fig. 9 (continued)
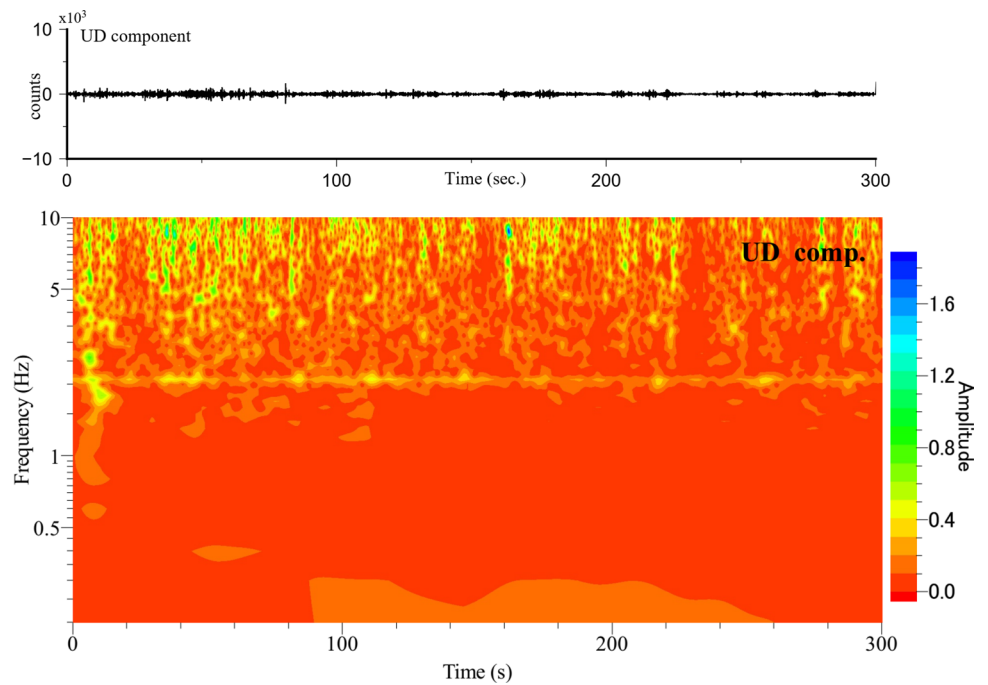
EHVSR curves are used as input in the diffuse field inversion process; consequently, the geometrically averaged inverted EHVSR curves are resulted. Reasonable fitting could be achieved after several trials and several inputting initial velocity structures in lighting by Kebeasy et al. (1991) and Mohamed et al. (2015) (Table 2). Fig. 12 is exhibiting the theoretical vertical and horizontal transfer functions (i.e., PP and SH, respectively). Three amplification patterns could be categorized based on these transfer functions. The first pattern is high amplifications as in MABD, NKUR, and NNMR stations around 3 Hz, 1.5 Hz, and 7 Hz, respectively. These amplifications could be related to the back-calculated velocity structures beneath each station. However, NNMR station is surrounded or in captive by NS faults (i.e., Kurkur and El-Baraqa faults) and EW Seiyal active fault. Consequently, its high amplification could be related to the constructive interference among incident seismic waves (i.e., generation of guided waves). The second pattern is medium amplifications as in MSM, NAHD, NGAL, NGMR, NMAN, NNAL, NSKD, and NWAL stations. In the literature (e.g., Li et al. 2004, Korneev et al. 2003, to cite few among many others), the seismogenic active faults of depths less than 10 km could work as fault zone waveguide, which is in agreement with the present study seismogenic earthquakes and their relevant resulting amplifications. The third pattern is low

amplifications as in NGRW station. Fig. 13 shows the back-calculated subsurface velocity structures (i.e., P-wave and S-wave velocities) at these 12 earthquake stations. Diffuse field inversion has been done on microtremor measurement sites A and C, and the resulting back-calculation MHVSR curves and their corresponding subsurface velocity structures are exhibited in Fig. 14.

The seismic bedrock is identified using the impedance contrast characteristics of S-wave and P-wave velocities (Thabet 2019 and 2021a), because these studies are applied and concluded based on 1743 sites with high variety of geological, lithological, and structural conditions. Equations 6 and 7 are defining the impedance contrast characteristics of S-wave and P-wave as IC_P and IC_S, respectively. Moreover, seismic bedrock corresponds to S-wave velocity of ≥ 3000 m/s (Kawase et al. 2011). Applying a Poisson's ratio of 0.25 for this seismic bedrock means P-wave velocity of ≥ 5200 m/s. Table 4 is summarizing the P-wave and S-wave velocities of the seismic bedrock and the average overlying layers beneath each station and site. Considering the achieved results from the earthquake stations, the averages of S-wave and P-wave velocities are 1394 ± 127 m/s and 2699 ± 369 m/s for the overlying layers and 3305 ± 225 m/s and 6575 ± 361 m/s for the seismic bedrock, respectively.
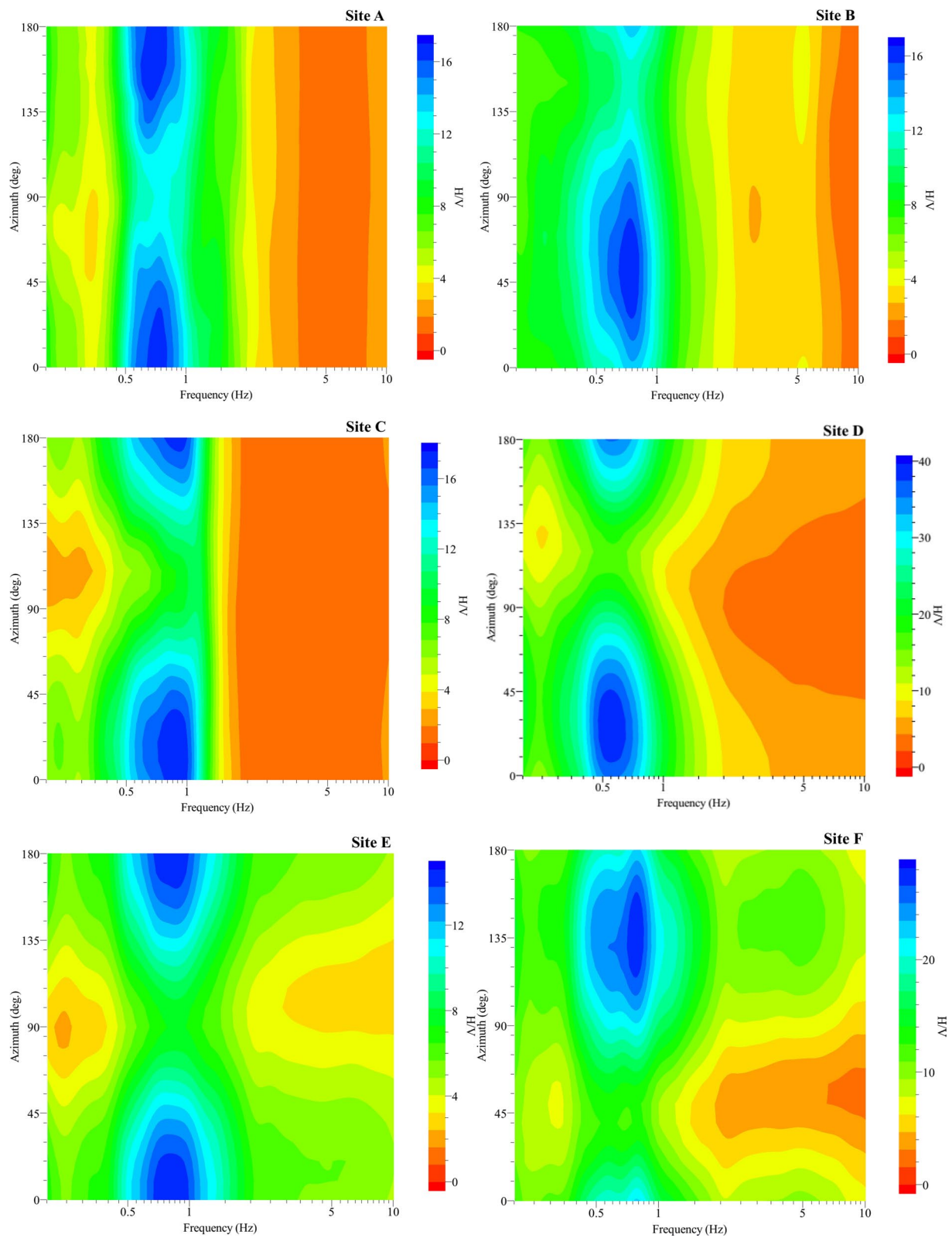
Fig. 10 Rotational MHVSRs at the 6 microtremor measurement sites

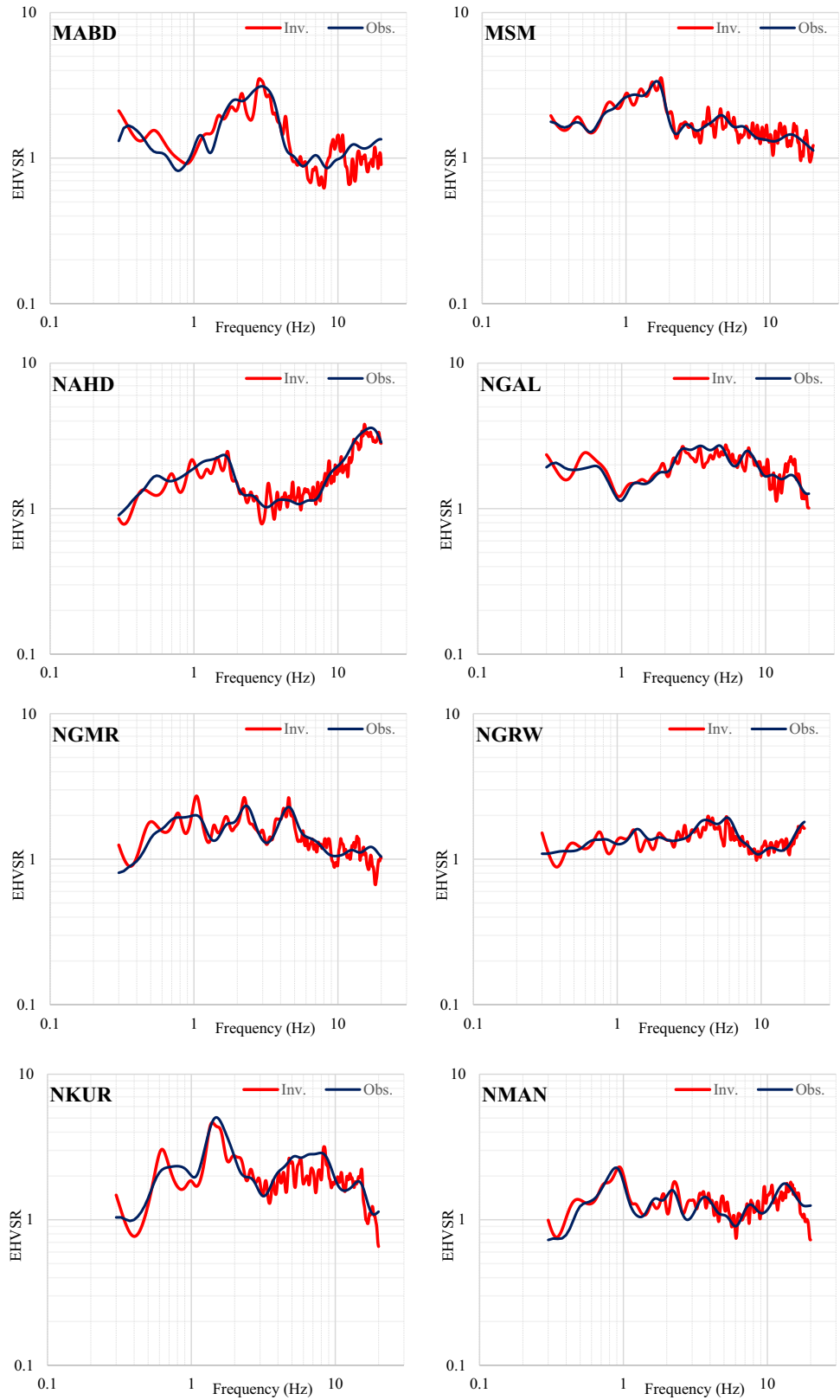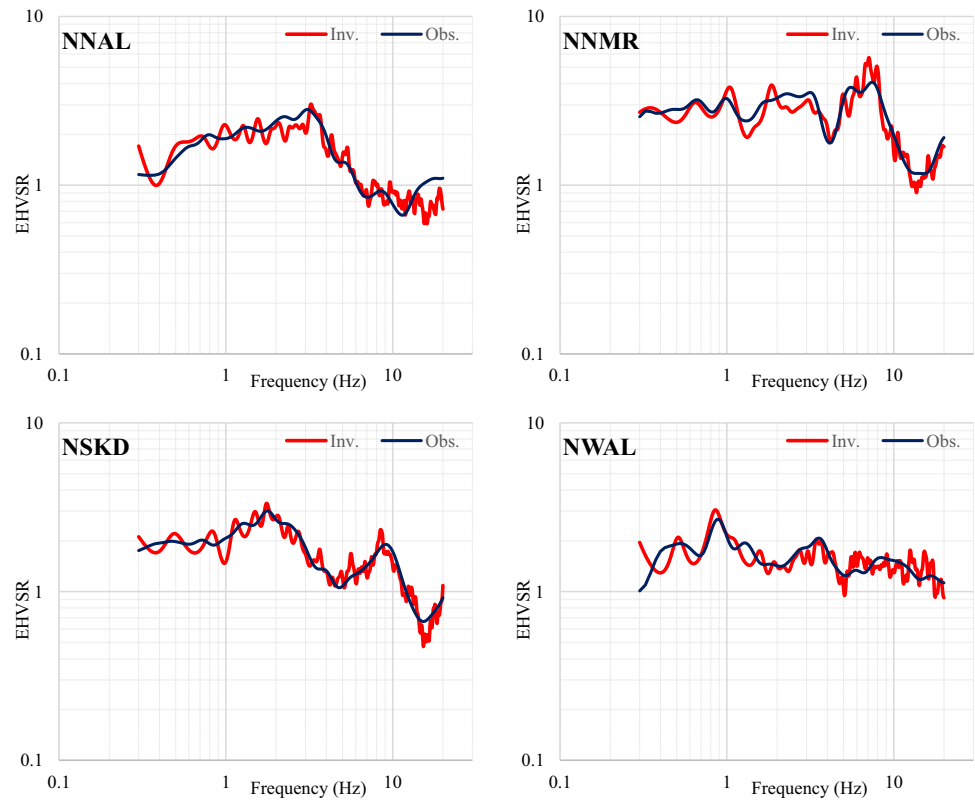**Fig. 11** Observed and inverted EHVSR curves at the 12 earthquake stations

Fig. 11 (continued)

$$IC_P = \frac{(\rho V_P)_{i+1} - (\rho V_P)_i}{(\rho V_P)_{i+1} + (\rho V_P)_i} \qquad (6)$$

$$IC_S = \frac{(\rho V_S)_{i+1} - (\rho V_S)_i}{(\rho V_S)_{i+1} + (\rho V_S)_i}, \qquad (7)$$

where ρ is the density of each layer i (note: 1 is the surficial layer and ith for underlying layers).

The different seismic site classes in Aswan region are associated through high variability of the overlying layers velocities. Although the initial velocities used in the diffuse field inversion are based on velocities obtained from Kebeasy et al. (1991) and Mohamed et al. (2015) (Table 2), our achieved velocities are significantly different. The inversion of an MHVSR or EHVSR curve has an important non-uniqueness problem (See Piña-Flores et al. 2017). For that purpose, the reliability of the present achieved subsurface velocity structures is proven due to the following four factors. First is the reasonable fitting between the observed and inverted EHVSR

curves. Second is the slight variability of the seismic bedrock velocities ($V_s \approx 3305 \pm 225$ m/s, and $V_p \approx 6575 \pm 361$ m/s) for the 12 different earthquake stations, although the search space is set to $\pm 300\%$ of the initial velocity structures. Additionally, these resulted seismic bedrock velocities agree with previous results by Kawase et al. 2011. This also indicates that diffuse field inversion process is reliable. As shown in Fig. 15, the third factor is the superimposing back-calculated velocity structures beneath NKUR station on the geologic 2D cross section (GG' line in Fig. 3), which is obtained from Mekkawi et al. (2005). The top 100 m layers are interpreted as weathered sandstone and shale (Nubian formation) and have averages V_s and V_p of 425 and 1491 m/s, respectively. Till depth of 345 m, un-weathered sandstone and shale (Nubian formation) have averages V_s and V_p of 1036 and 1757 m/s, respectively. The seismic bedrock, which is composed of Precambrian metamorphic and plutonic rocks, has V_s and V_p of 3342 and 6753 m/s, respectively. Fourth is detecting the presence of groundwater from back-calculated velocity structures taking advantage of the seismic reflectivity parameter (*SRP*), which is defined by

Fig. 12 Horizontal and vertical (i.e., SH and PP, respectively) theoretical transfer functions at the 12 earthquake stations
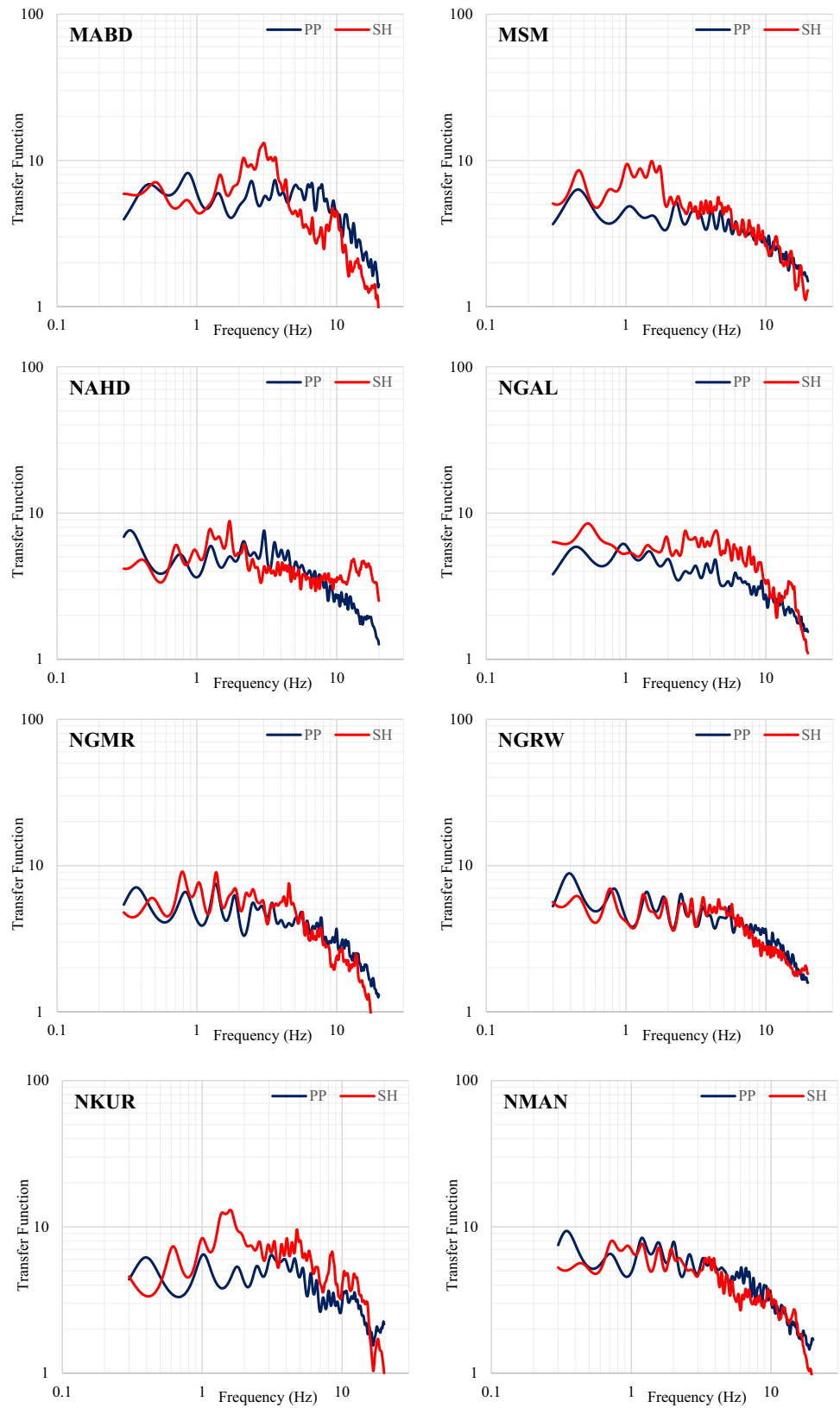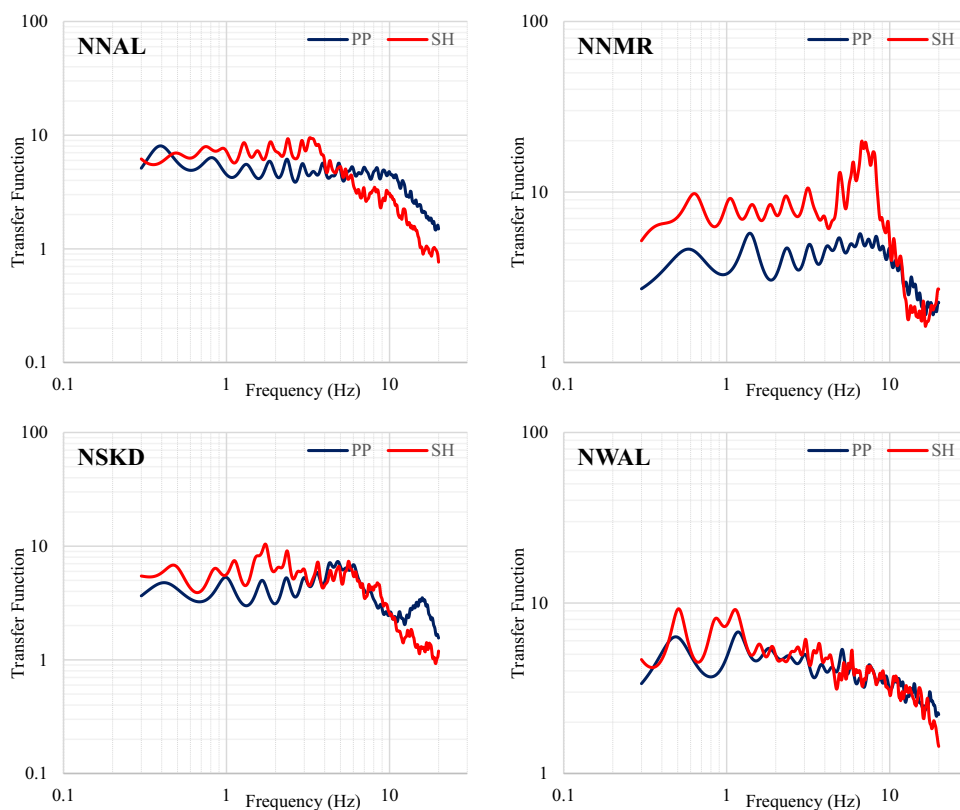
Fig. 12 (continued)

Thabet 2021b (see Eq. 8). The presence of groundwater is judged by the high SRP values, otherwise close to zero or negative *SRP* values are considered as lithological variations. The zero *SRP* is indicating inter-layer condition. For this purpose, we used the groundwater data of the piezometric network constructed and installed by the High and Old Aswan Dams Authority (HADA) in cooperation with the National Research Institute of Astronomy and Geophysics. Two boreholes are in the vicinity of NNMR station, whereas seven boreholes are in the vicinity of NGMR station (i.e., 1–2 and 3–9, respectively, in Fig. 3). The theoretical groundwater level at NNMR station is 41 m and 440 m, as determined by SRP index. This estimation is similar to the observed groundwater levels in boreholes 1–2, which are ranging between 49.5 m and 56.5 m. On the other hand, the theoretical groundwater levels at NGMR station are 18 m and 219 m, whereas the observed groundwater levels in boreholes 3–9 are ranging between 71.2 m and 85.4 m. Although the present resulting subsurface velocity structures are considered as reliable, but

these back-calculated velocities are nonunique satisfactory velocity structures (Fig. 16).

$$\text{SPR} = IC_\text{P} - IC_\text{S}, \tag{8}$$

where IC_P and IC_S are defined in Eqs. 6 and 7.

Conclusion

This study provides an updated database for the seismic site characterization of fourteen earthquake stations, which belong to the Egyptian National Seismic Network (ENSN) and located in Aswan area, as well as six microtremor measurement sites in the vicinity of the High Dam. Earthquake and microtremor analyses of EHVSRs and MHVSRs, respectively, accompanied with their rotated plots were performed to obtain resonance frequencies and the dominant amplification directions. The subsurface velocity structures beneath these stations and sites were
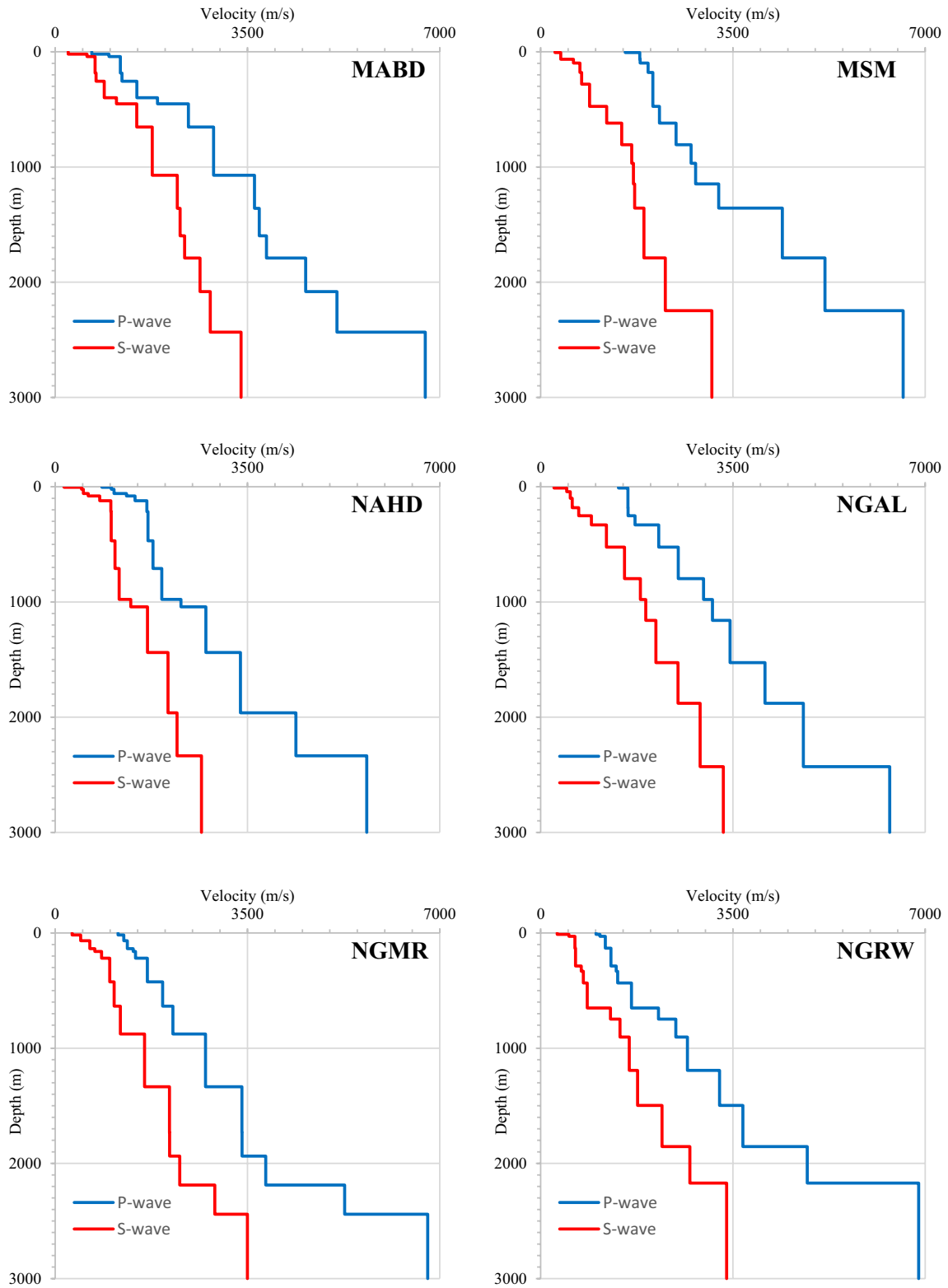
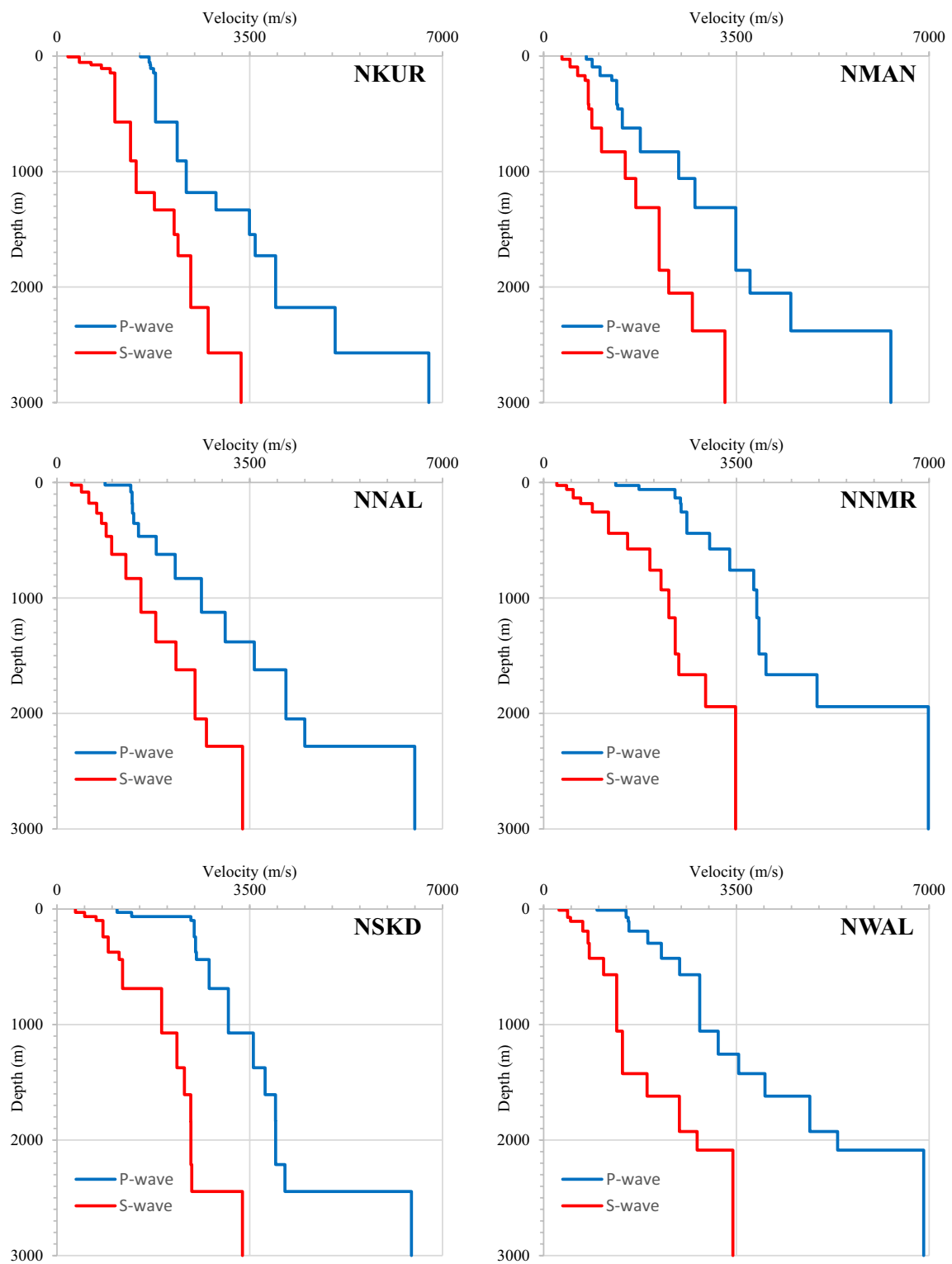Fig. 13 Back-calculated velocity structures at the 12 earthquake stations
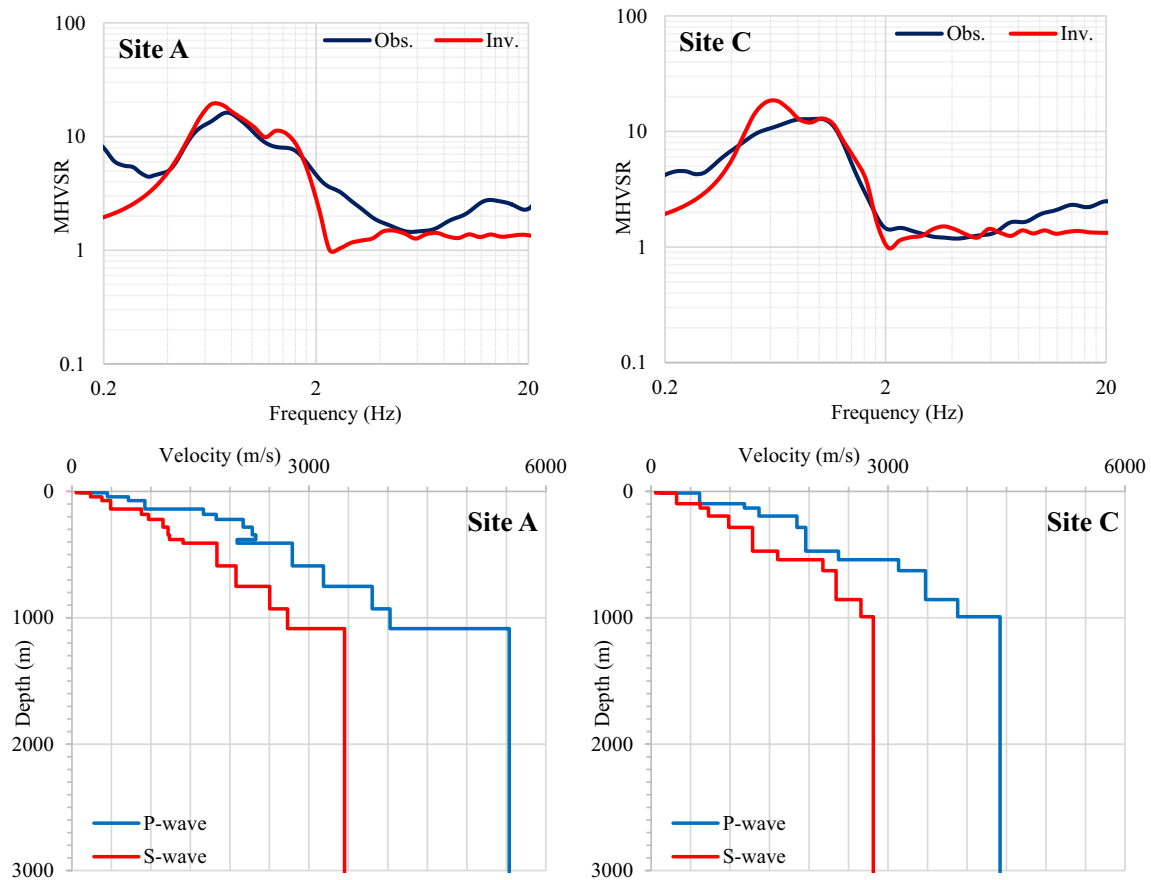
Fig. 13 (continued)

Fig. 14 Observed and inverted MHVSR curves at sites A and C (upper panels), and their back-calculated velocity structures (lower panels)

Table 4 Summary of characteristics of the seismic bedrock and its corresponding overlying layers

Sta	Depth to seismic bedrock (m)	Overlying layers averages (m/s)		Seismic bedrock (m/s)	
		V_s	V_p	V_s	V_p
MABD	2433	1572	2671	3384	6737
MSM	2247	1311	2964	3115	6600
NAHD	2335	1357	2347	2663	5670
NGAL	2429	1529	2922	3324	6354
NGMR	2441	1392	2527	3500	6781
NGRW	2170	1243	2295	3386	6881
NKUR	2570	1499	2705	3342	6753
NMAN	2380	1277	2154	3291	6306
NNAL	2284	1288	2414	3370	6497
NNMR	1940	1483	3361	3486	6986
NSKD	2445	1555	3169	3367	6436
NWAL	2087	1228	2867	3436	6901
Site A	1085	954	1667	3451	5537
Site C	991	903	1564	2814	4418

determined using diffuse field concept of both earthquake scheme (Kawase et al. 2011; Nagashima et al. 2014) and microtremor scheme (Sánchez-Sesma et al. 2011a). The diffuse field inversion successfully and suitably retrieved the velocity structures in 12 earthquake stations and 2 microtremor measurement sites but failed in 2 stations and 4 sites due to SNRs < 2, and noise of industrial origin (i.e., High Dam), respectively. The authors recommend much complex microtremor measurements in the vicinity of megastructures in the study area.

We observed that EHVSRs revealed dominant polarization in EW and NE–SW directions in the frequency range between 0.5 and 10.0 Hz, whereas MHVSRs revealed dominant polarization in NS and NE–SW directions in the frequency range between 0.3 and 1.0 Hz. These dominant polarization directions are near-transversal – transversal to the EW and NS main strikes of the active fault system, respectively. The near-transversal – transversal relationship between the amplification directions which are resulting at both the 14 earthquake stations and the
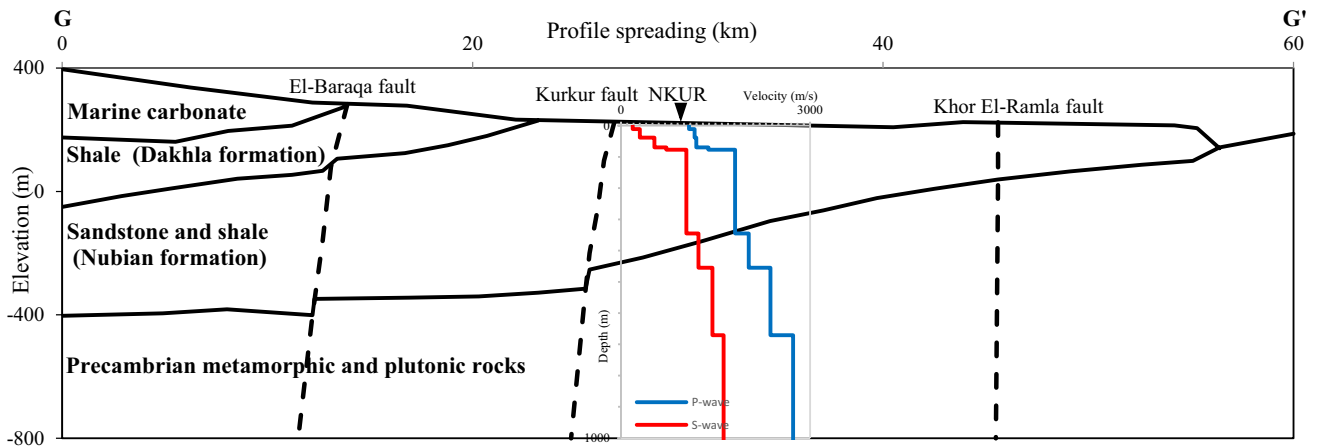
Fig. 15 Superimposition of subsurface velocity structure beneath NKUR station on the geological 2D cross section (i.e., GG' line in Fig. 3) obtained from Mekkawi et al. (2005)
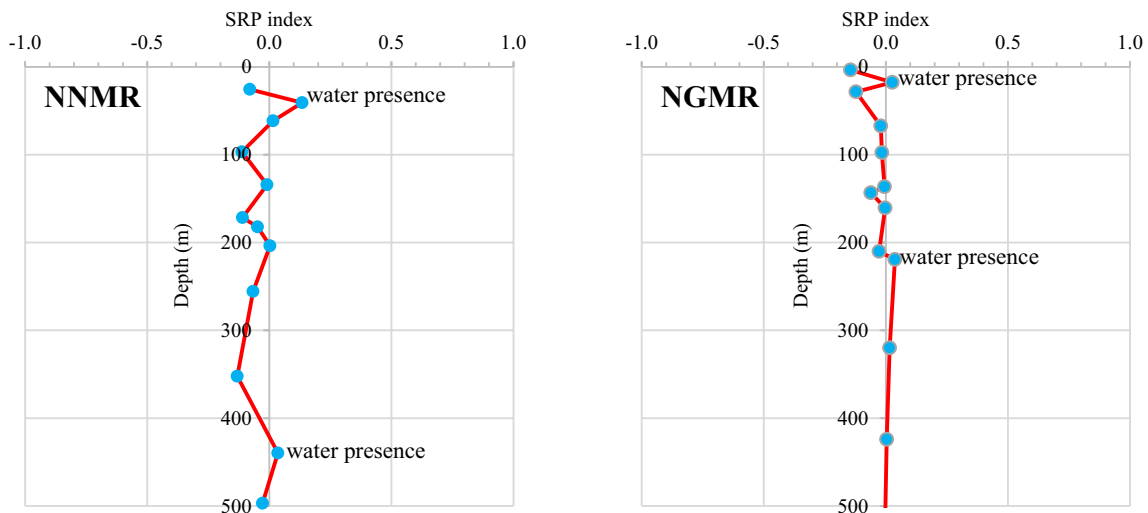

Fig. 16 Groundwater presence using SRP index (Thabet 2021b) at NNMR and NGMR stations

6 microtremor measurement sites, and the active fault system in the study area is in agreement with Pischiutta et al. (2017), Panzera et al. (2019), Tortorici et al. (2019), and Kakhki et al. (2020), to cite few among many others. The difference between the EHVSRs and MHVSRs is attributed to the different nature of the wavefield for the earthquakes and microtremors.

The discussed results and methods demonstrate the utility of the need to continuously update the seismic site characterization for the Egyptian National Seismic Network stations, particularly those in the near vicinity of megastructures in Egypt.

Declarations

Conflict of interest The authors declare that they have no known competing financial interests or personal relationships which have or could be perceived to have influenced the work reported in this article.

Ethics approval This work does not involve the use of human subjects, does not involve animal experiments, and does not involve data collected from social media platforms.

References

Bard PY, SESAME team (2004) Guidelines for the implementation of the H/V spectral ratio technique on ambient vibrations: measurements, processing and interpretation, SESAME European research project, WP12—Deliverable D23. 12, http://sesame-fp5.obs.ujfgrenoble.fr/Deliverables

Ben-Zion Y (1998) Properties of seismic fault zone waves and their utility for imaging low-velocity structure. J Geophys Res 103(12):567–585

Ben-Zion Y, Aki K (1990) Seismic radiation from an SH line source in a laterally heterogeneous planar fault zone. Bull Seismol Soc Am 80:971–994

Bonnefoy-Claudet S, Köhler A, Cornou C, Wathelet M, Bard PY (2008) Effects of love waves on microtremor H/V ratio. Bull Seismol Soc Am 98:288–300. https://doi.org/10.1785/0120070063

Burjánek J, Moore JR, Yugsi-Molina FX, Fäh D (2012) Instrumental evidence of normal mode rock slope vibration. Geophys J Int 188(2):559–569. https://doi.org/10.1111/j.1365-246X.2011.05272.x

Di Giulio G, Cara F, Rovelli A, Lombardo G, Rigano R (2009) Evidences for strong directional resonances in intensely deformed zones of the Pernicana fault, Mount Etna, Italy. J Geophys Res 114:B10308. https://doi.org/10.1029/2009JB006393

Douglas J, Gehl P, Bonilla LF, Ge´lis C (2010) AJ model for mainland France. Pure Appl Geophys 167:1303–1315. https://doi.org/10.1007/s00024-010-0146-5

EGSMA (Egyptian Geological Survey and Mining Authority), (1981) Geological map of Egypt scale1:2000000 EGSMA, Ministry of Industry and Mineral Resources, Cairo.

Fäh D, Kind F, Giardini D (2001) A theoretical investigation of average H/V ratios. Geophys J Int 145:535–549. https://doi.org/10.1046/j.0956-540x.2001.01406.x

Field EH, Jacob KH (1995) A comparison and test of various site-response estimation techniques, including three that are not reference-site dependent. Bull Seismol Soc Am 85(4):1127–1143

Fohrmann M, Igel H, Jahnke G, Ben-Zion Y (2004) Guided waves from sources outside faults: an indication for shallow fault zone structure? Pure Appl Geophys 161:2125–2137

García-Jerez A, Piña-Flores J, Sánchez-Sesma FJ, Luzón F, Perton M (2016) A computer code for forward computation and inversion of the H/V spectral ratio under the diffuse field assumption. Comput Geosci 97:67–78

Guiraud RO, Bosworth W (1999) Phanerozoic geodynamic evolution of northeastern Africa and the northwestern Arabian platform. Tectonophysics 315(1):73–104

Hamimi Z, Hagag W, Osman R, El-Bialy M, Abu El-Nadr I, Fadel M (2018) The active Kalabsha fault zone in Southern Egypt: detecting faulting activity using field-structural data

and EMR-technique, and implications for seismic hazard assessment. Arab J Geosci 11:421. https://doi.org/10.1007/s12517-018-3774-1

Hickman SH, Zoback MD, Ellsworth WL (2005) Structure and composition of the San Andreas fault zone at Parkfield: initial results from SAFOD Phase 1 and 2 EOS. Trans Am Geophys Union 83(47):237

Igel H, Ben-Zion Y, Leary P (1997) Simulation of *SH* and *P-SV* wave propagation in fault zones. Geophys J Int 128:533–546

Issawi B (1978) Geology of Nubia west area Western Desert, Egypt. Ann Geol Surv Egypt 8:237–253

Issawi B (1968) The geology of Kurkur-Dungle area Geol. survey, Cairo, Egypt, paper No. 46, 102.

Kakhki MK, Peters FC, Mansur WJ, SadidKhoii A, Rezaei S (2020) Deciphering site response directivity in landslide-prone slopes from ambient noise spectral analysis. Eng Geol 269:105542. https://doi.org/10.1016/j.enggeo.2020.105542

Kawase H, Sánchez-Sesma FJ, Matsushima S (2011) The optimal use of horizontal-tovertical (H/V) spectral ratios of earthquake motions for velocity structure inversions based on diffuse field theory for plane waves. Bull Seism Soc Am 101(5):2001–2014. https://doi.org/10.1785/0120100263

Kebeasy RM, Bayoumy AI, Gharib AA (1991) Crustal structure modeling for the northern part of the Aswan Lake area using seismic waves generated by and local earthquakes. J Geodyn 14(1–4):159–182

Kim J, Sultan M (2002) Assessment of the long-term hydrologic impacts of Lake Nasser and related irrigation projects in Southwestern Egypt. J Hydrol 262(1–4):68–83. https://doi.org/10.1016/S0022-1694(02)00013-6

Konno K, Ohmachi T (1998) Ground-motion characteristics estimated from spectral ratio between horizontal and vertical components of microtremor. Bull Seismol Soc Am 88:228–241

Korneev VA, Nadeau RM, McEvilly TV (2003) Seismological studies at Parkfield IX: fault-zone imaging using guided wave attenuation. Bull Seism Soc Am 93:1415–1426

Lermo J, Chávez-García FJ (1994) Are Microtremors useful in site response Evaluation? Bull Seismol Soc Am 84(5):1350–1364

Li YG, Leary PC, Aki K, Malin P (1990) Seismic trapped modes in the Orville and san Andreas fault zones. Science 249:763–766

Li YG, Aki K, Adams D, Hasemi A, Lee WHK (1994) Seismic guided waves trapped in the fault zone of the Landers, California, earthquake of 1992. J Geophys Res 99:11705–11722

Li YG, Ellsworth WL, Thurber CH, Malin PE, Aki K (1997) Fault zone guided waves from explosions in the San Andreas fault at Parkfield and Cienega Valley California. Bull Seism Soc Am 87:210–221

Li YG, Vidale JE, Cochran ES (2004) Low-velocity damaged structure of the San Andreas fault at Parkfield from fault zone trapped waves. Geophys Res Lett 31:L12S06. https://doi.org/10.1029/2003GL019044

Margerin L, Campillo M, Van Tiggelen BA, Hennino R (2009) Energy partition of seismic coda waves in layered media: theory and application to Pinyon Flats Observatory. Geophys J Int 177(2):571–585

Mekkawi M, Schnegg PA, Hamed TA, Elathy E (2005) Electrical structure of the tectonically active Kalabsha fault Aswan, Egypt. Earth Planet Sci Lett 240:764–773. https://doi.org/10.1016/j.epsl.2005.09.035

Mohamed A, Lindholm C, Girgis M (2015) Site characterization and seismic site response study of the Sahary Area South Egypt. Acta Geodyn Geomater 12(180):427–436

Mori Y, Matsushima S, Kawase H, Nagashima F (2015) Comparison of observed earthquake and microtremor horizontal-to-vertical spectral ratios and inversion of velocity structures based on their

empirical ratios. J Jpn Assoc Earthq Eng 16(9):13–32 (**[in Japanese with English abstract]**)

Nagashima F, Matsushima S, Kawase H, Sánchez-Sesma FJ, Hayakawa T, Satoh T, Oshima M (2014) Application of horizontal-to-vertical (H/V) spectral ratios of earthquake ground motions to identify subsurface structures at and around the K-NET site in Tohoku, Japan. Bull Seism Soc Am 104:2288–2302. https://doi.org/10.1785/0120130219

Omar KhA, El-Amin EM, Dahy SA, Ebraheem MO (2019) A study on the relation between recent induced seismicity and water level in the Northwestern part of Nasser lake Aswan—Egypt. Geotectonics 53(2):251–259. https://doi.org/10.1134/S0016852119020067

OJ Ktenidou (2010) Experimental and theoretical study of seismic ground motion in the city of Aegion, Greece, focusing on local site and topographic effects, PhD thesis, Department of Civil Engineering, Aristotle University Thessaloniki, Greece, http://invenio.lib.auth.gr/record/124050/files/GRI-2010-5489.pdf

Panzera F, Lombardo G, Longo E, Langer H, Branca S, Azzaro R, Cicala V, Trimarchi F (2017) Exploratory seismic site response surveys in a complex geologic area: a case study from Mt. Etna volcano (southern Italy). Nat Hazards 86:385–399. https://doi.org/10.1007/s11069-016-2517-4

Panzera F, D'Amico S, Colica E, Viccaro M (2019) Ambient vibration measurements to support morphometric analysis of a pyroclastic cone. Bull Volcanol 81(12):74. https://doi.org/10.1007/s00445-019-1338-1

Panzera F, Tortorici G, Romagnoli G, Marletta G, Catalano S (2020) Empirical evidence of orthogonal relationship between directional site effects and fracture azimuths in an active fault zone: the case of the Mt Etna lower eastern flank. Eng Geol 279:105900. https://doi.org/10.1016/j.enggeo.2020.105900

Piña-Flores J, Perton M, García-Jerez A, Carmona E, Luzón F, Molina-Villegas JC, Sánchez-Sesma FJ (2017) The inversion of spectral ratio H/V in a layered system using the diffuse field assumption (DFA). Geophys J Int 208(1):577–588

Piña-Flores J, Cárdenas-Soto M, García-Jerez A, Campillo M, Sánchez-Sesma FJ (2021) The search of diffusive properties in ambient seismic noise. Bull Seismol Soc Am 111:1650–1660

Pischiutta M, Fondriest M, Demurtas M, Magnoni F, Di Toro G, Rovelli A (2017) Structural control on the directional amplification of seismic noise (Campo Imperatore, Central Italy). Earth Planet Sci Lett 471:10–18. https://doi.org/10.1016/j.epsl.2017.04.017

Rigano R, Cara F, Lombardo G, Rovelli A (2008) Evidence of ground motion polarization on fault zones of Mount Etna volcano. J Geophys Res 113:B10306. https://doi.org/10.1029/2007JB005574

Sánchez-Sesma FJ, Rodríguez M, Iturrarán-Viveros U, Luzón F, Campillo M, Margerin L, García-Jerez A, Suarez M, Santoyo MA, Rodríguez-Castellanos A (2011a) A theory for microtremor H/V spectral ratio: application for a layered medium. Geophys J Int Exp Lett 186(1):221–225. https://doi.org/10.1111/j.1365-246X.2011.05064.x

Sánchez-Sesma FJ, Weaver RL, Kawase H, Matsushima S, Luzón F, Campillo M (2011b) Energy partitions among elastic waves for dynamic surface loads in a semi-infinite solid. Bull Seismol Soc Am 101(4):1704–1709

Shapiro NM, Campillo M, Margerin L, Singh SK, Kostoglodov V, Pacheco J (2000) The energy partitioning and the diffusive character of the seismic coda. Bull Seismol Soc Am 90:655–665

Stern RJ, Abdelsalam MG (1996) The origin of the great bend of the Nile from SIR-C/X-SAR imagery. Science 274(5293):1696–1698. https://doi.org/10.1126/science.274.5293.1696

Thabet M (2019) Site-specific relationships between bedrock depth and hvsr fundamental resonance frequency using KiK-NET data from Japan. Pure Appl Geophys 176:4809–4831. https://doi.org/10.1007/s00024-019-02256-7

Thabet M (2021a) Improved site-dependent statistical relationships of VS and resonant frequency versus bedrock depth in Japan. J Seismol 25:1441–1459. https://doi.org/10.1007/s10950-021-10038-9

Thabet M (2021b) Applicability of a proposed groundwater level determination approach for the K-NET in Japan. Near Surf Geophys 19(4):447–463. https://doi.org/10.1002/nsg.12162

Thurmond AK, Allison K, Stern RJ, Mohamed G, Abdelsalam MG, Kent D, Nielsen C, Abdeen MM, Hinz E (2004) The Nubian swell. J Afr Earth Sci 39:401–407

Tortorici G, Romagnoli G, Grassi S, Imposa S, Lombardo G, Panzera F, Catalano S (2019) Quaternary negative tectonic inversion along the sibillini Mts. Thrust zone: the arquata del tronto case history (Central Italy). Environ Earth Sci 78(1):37. https://doi.org/10.1007/s12665-018-8021

Villani F, D'Amico S, Panzera F, Vassallo M, Bozionelos G, Farrugia D, Galea P (2018) Shallow high-resolution geophysical investigation along the western segment of the victoria lines fault (Island of Malta). Tectonophysics 724–725:220–233. https://doi.org/10.1016/j.tecto.2018.01.010

Wathelet M, Chatelain J-L, Cornou C, Di Giulio G, Guillier B, Ohrnberger M, Savvaidis A (2020) Geopsy: a user-friendly open-source tool set for ambient vibration processing. Seismol Res Lett 91(3):1878–1889. https://doi.org/10.1785/0220190360

Weaver RL (1985) Diffuse elastic waves at a free surface. J Acoust Soc Am 78(1):131–136

Woodward-Clyde (1985) Identification of earthquake sources and estimation of magnitudes and recurrence intervals. Internal Report High and Aswan Dams Authority